



Simulation of mean flow and turbulence over a 2D building array using high-resolution CFD and a distributed drag force approach

F.S. Lien^a, E. Yee^{b,*}, Y. Cheng^a

^a *Department of Mechanical Engineering, University of Waterloo, Waterloo, Canada*

^b *Defence R&D Canada – Suffeld, Medicine Hat, P.O. Box 4000, Alberta, Canada T1A 8K6*

Abstract

A numerical simulation has been performed of the disturbed flow through and over a two-dimensional array of rectangular buildings immersed in a neutrally stratified deep rough-walled turbulent boundary-layer flow. The model used for the simulation was the steady-state Reynolds-averaged Navier–Stokes equations with linear and non-linear eddy viscosity formulations for the Reynolds stresses. The eddy viscosity was determined using a high-Reynolds number form of the $k-\epsilon$ turbulence-closure model with the boundary conditions at the wall obtained with a standard wall-function approach. The resulting system of partial differential equations was solved using the SIMPLE algorithm in conjunction with a non-orthogonal, colocated, cell-centered, finite volume procedure. The predictive capabilities of the high-resolution computational fluid dynamics (CFD) simulations of urban flow are validated against a very detailed and comprehensive wind tunnel data set. Vertical profiles of the mean streamwise velocity and the turbulence kinetic energy are presented and compared to those measured in the wind tunnel simulation.

It is found that the performance of all the turbulence models investigated is generally good—most of the qualitative features in the disturbed turbulent flow field through and over the building array are correctly reproduced. The quantitative agreement is also fairly good (especially for the mean velocity field). Overall, the non-linear $k-\epsilon$ model gave the best performance among four different turbulence closure models examined. The turbulence energy levels within the street canyons and in the exit region downstream of the last building were underestimated by all four turbulence closure models. This appears to contradict the ‘stagnation point anomaly’ associated with the standard $k-\epsilon$ model which is a result of the excessive turbulence energy production due to normal straining. A possible explanation for this is the inability of the present models to account properly for the effects of secondary

*Corresponding author. Tel.: 403-544-4605; fax: 403-544-3388.

E-mail address: eugene.yee@drdc-rddc.gc.ca (E. Yee).

strains on the turbulence and/or for the effects of large-scale flapping of the strong shear layer at the canopy top.

The results of the high-resolution CFD simulations have been used to diagnose values of the drag coefficient to be used in a distributed drag force representation of the obstacles in the array. Comparisons of the measured spatially-averaged time-mean mean velocity and turbulence kinetic energy in the array with predictions of the disturbed flow using the distributed drag force approach have been made.

© 2003 Elsevier Ltd. All rights reserved.

Keywords: Building clusters; Turbulence modeling; Drag coefficient prediction

1. Introduction

In recent years, a great effort has been made to understand the impact of large numbers of discrete bluff obstacles (e.g., buildings, trees, and other obstructions in a prescribed domain within a large city) on the atmospheric boundary-layer flow because of its importance in many aspects of meteorology, wind engineering, and environmental science. In particular, how the speed, direction, and turbulence of the wind changes as it blows through a cluster of buildings must be known if the mean transport and turbulent diffusion of airborne contaminants in its vicinity are to be determined. Furthermore, knowledge of the velocity and pressure distributions near the inlets and outlets of heating and ventilating systems of buildings is required to determine the egress of contaminants into buildings. Indeed, in response to increasing concerns on the use of chemical, biological, and radiological materials against populations in urban areas, there has been a concerted effort by a number of government, military, and civilian research laboratories and agencies in recent years to develop models that can predict the turbulent flow and dispersion in urban (built-up) areas.

As far as numerical modeling of flows round obstacles is concerned, most of the effort has been concentrated on modeling the flow around isolated structures or single buildings rather than around groups of obstacles or building clusters. Prognostic models that solve the Reynolds-averaged Navier–Stokes (RANS) equations have been used to describe the flow field around an isolated cuboid or building (see Refs. [1–4]) or the interaction of two buildings [5]. These models used the simple $k-\epsilon$ turbulence model in the RANS equations to determine the mean flow and turbulence and, hence, were basically non-linear flow models solved using either finite difference, finite element, or finite volume solution techniques. Computational fluid dynamics (CFD) models have also been applied to describe the flow within a specific urban structure (e.g., urban street canyon). In particular, Hunter et al. [6] used the $k-\epsilon$ model of turbulence to describe the three-dimensional characteristics of flow regimes within an urban canyon.

The most complicated flow problem is arguably that of a large building cluster consisting of a group of buildings of roughly comparable size with the spacing between buildings sufficiently close that the flow round any individual building in the

cluster is being influenced by all other buildings in its neighborhood (e.g., see the discussion provided by Hosker [7]). Generally speaking, urban flow and dispersion within various arrays of obstacles are addressed on a case-by-case basis. From a theoretical point of view, the problem appears to be complex and unwieldy and there appears to be no idealized starting point for analysis. From an application point of view, it is easy to get lost in the complexities of particular cases without ever having to see that there might be a common physical picture of mean flow and turbulence characteristics in various building cluster configurations. However, from a numerical viewpoint, it appears that numerical simulation models based on RANS equations are general enough to be applied *mutatis mutandi* to the problem of disturbed flow within general building cluster configurations where mutual flow interferences between buildings need to be taken into account. The principal problem with the application of such CFD models to building arrays is that there is currently very little benchmark mean flow and turbulence data that could be used to compare with the model predictions. It is crucial that before any CFD model with its attendant turbulence closure is applied to a particular class of problems (e.g., flow through building array), that the model predictions are subjected first to critical and comparative judgements against high-quality data sets before such model predictions are taken as “ground truth”.

In this paper, we use the $k-\epsilon$ model of turbulence within the RANS modeling framework to simulate the developing flow through and over a two-dimensional (2D) array of surface mounted obstacles immersed within a deep rough-walled turbulent boundary-layer under neutrally stratified flow. We show a detailed comparison with a wind tunnel experiment of the mean flow field and turbulence kinetic energy for this obstacle array. In addition to the high-resolution CFD simulation, we investigate the utility of neglecting the detailed structure of the solid boundaries of the obstacles in the array and considering them simply as an aggregate effect (viz., we consider the aggregation of groups of buildings in the array and describe them simply by a distributed drag force on the airflow entering the array).

2. The wind tunnel experiment

The wind tunnel experiment is fully described in Ref. [8] and only the important details of the experiment will be presented here. The experiments were conducted in an open-return type wind tunnel at the US Environmental Protection Agency's Fluid Modeling Facility. This wind tunnel has a working test section of length 18.3 m, width 3.7 m, and an adjustable roof of height approximately 2.1 m to eliminate streamwise pressure gradients and allow for a non-accelerating free stream flow.

A schematic of the two-dimensional building array used for these wind tunnel experiments is shown in Fig. 1. This array consisted of seven rectangular blocks, each block with equal height, H , and length, L , of 150 mm. The blocks were spaced H apart in the streamwise direction. The building array was immersed in a simulated neutral atmospheric boundary layer which was created in the wind tunnel using spires and floor roughness with a roughness length of approximately 1 mm. The

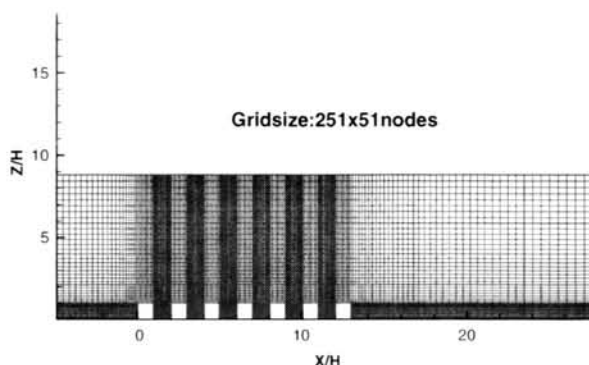


Fig. 1. Computational grid superimposed on the flow domain used for the high-resolution numerical simulation of the two-dimensional (2D) array of buildings.

mean streamwise velocity in the upstream approach flow can be approximated by the following power-law form:

$$\frac{\bar{u}(z)}{\bar{u}_H} = \left(\frac{z}{H}\right)^{0.16}, \quad (1)$$

where $\bar{u}_H = 3 \text{ m s}^{-1}$ is the reference velocity at $z = H$. The Reynolds number, based on the building height H and the reference velocity \bar{u}_H , is 30,000.

The streamwise, cross-stream (or, spanwise), and vertical velocity components were measured with a pulsed-wire anemometer using a pulsing rate of 10 Hz and a sampling time of 120 s at each measurement location. The pulsed-wire anemometer, unlike a standard X-array hot-wire anemometer, can be used to measure velocities in high intensity turbulence with reversing flows such as those which exist within an obstacle array. Measurements of the three components of the instantaneous velocity were made at 1016 coordinate positions. These measurements consisted of 81 vertical profiles of mean velocity, turbulence velocity variance, and turbulence kinetic energy. These profiles extended from $3.5H$ upstream of the first building to $7.5H$ downstream of the last building. Each vertical profile consisted of either 8 (over the rooftops) or 16 (over the urban canyons, and either upstream or downstream of the array) measurement positions up to a vertical height of $3H$ above the ground surface. All streamwise distances are measured relative to the location of the upstream wall of the first building at $x/H = 0$.

3. High-resolution computational fluid dynamics

3.1. Mathematical model

The governing equations for the flow of an incompressible fluid at high Reynolds number (Re) based on the Reynolds-averaged Navier–Stokes approach are:

$$\frac{\partial \bar{u}_i}{\partial x_i} = 0, \quad (2)$$

$$\frac{\partial \bar{u}_i \bar{u}_j}{\partial x_j} = -\frac{1}{\rho} \frac{\partial \bar{p}}{\partial x_i} - \frac{\partial \overline{u'_i u'_j}}{\partial x_j}, \quad (3)$$

where the Reynolds averaging of a quantity is denoted by drawing a bar over the quantity. Here \bar{u}_i and u'_i are the mean and fluctuating velocities in the x_i -direction, respectively; ρ is the density of the fluid; and, \bar{p} is the dynamic pressure. In Eqs. (2) and (3), the Einstein summation convention is assumed. Subscripts 1–3 refer to directions along x (streamwise), y (spanwise), and z (vertical), respectively. Furthermore, $(u_1, u_2, u_3) \equiv (u, v, w)$.

The presence of the kinematic Reynolds stresses $\overline{u'_i u'_j}$ in the mean momentum equation [Eq. (3)] implies the latter is not closed. Closure requires that some approximation be made in prescribing the Reynolds stresses in terms of the mean flow quantities. A common closure approximation for $\overline{u'_i u'_j}$, first suggested by Pope [9], is

$$\begin{aligned} \overline{u'_i u'_j} = & \frac{2}{3} k \delta_{ij} - \nu_T \underbrace{\left(\frac{\partial \bar{u}_i}{\partial x_j} + \frac{\partial \bar{u}_j}{\partial x_i} \right)}_{\text{linear term}} \\ & + \underbrace{\frac{k^3}{\varepsilon^2} \left[C_{\tau 1} \left(\frac{\partial \bar{u}_i}{\partial x_k} \frac{\partial \bar{u}_j}{\partial x_k} \right)^* + C_{\tau 2} \left(\frac{\partial \bar{u}_i}{\partial x_k} \frac{\partial \bar{u}_k}{\partial x_j} + \frac{\partial \bar{u}_j}{\partial x_k} \frac{\partial \bar{u}_k}{\partial x_i} \right)^* + C_{\tau 3} \left(\frac{\partial \bar{u}_k}{\partial x_i} \frac{\partial \bar{u}_k}{\partial x_j} \right)^* \right]}_{\text{quadratic term}} \\ & + \text{HOT}, \end{aligned} \quad (4)$$

where δ_{ij} is the Kronecker delta symbol, HOT denotes higher-order terms, and '*' indicates the deviatoric part; for example,

$$\left(\frac{\partial \bar{u}_i}{\partial x_k} \frac{\partial \bar{u}_j}{\partial x_k} \right)^* = \frac{\partial \bar{u}_i}{\partial x_k} \frac{\partial \bar{u}_j}{\partial x_k} - \frac{1}{3} \frac{\partial \bar{u}_m}{\partial x_n} \frac{\partial \bar{u}_m}{\partial x_n} \delta_{ij}. \quad (5)$$

Furthermore, $k \equiv \frac{1}{2} \overline{u'_i u'_i}$ is the turbulence kinetic energy (TKE), ε is the rate of dissipation of turbulence kinetic energy, and ν_T is the kinematic eddy (turbulent) viscosity. In the conventional linear eddy-viscosity models (e.g. Refs. [10–12]), only the linear term is retained. For Shih et al.'s *quadratic* non-linear eddy-viscosity model [13], HOT is zero and

$$(C_{\tau 1}, C_{\tau 2}, C_{\tau 3}) = \left(\frac{13}{1000 + \tilde{S}^3}, \frac{-4}{1000 + \tilde{S}^3}, \frac{-2}{1000 + \tilde{S}^3} \right), \quad (6)$$

where

$$\tilde{S} \equiv \frac{\sqrt{2 S_{ij} S_{ij}} k}{\varepsilon}, \quad S_{ij} = \frac{1}{2} \left(\frac{\partial \bar{u}_i}{\partial x_j} + \frac{\partial \bar{u}_j}{\partial x_i} \right). \quad (7)$$

Here, \tilde{S} is the characteristic strain invariant constructed from the mean rate-of-strain tensor S_{ij} .

In the framework of $k-\varepsilon$ models, the eddy viscosity ν_T is given by

$$\nu_T = C_\mu \frac{k^2}{\varepsilon}, \quad (8)$$

where k and ε are determined from the following transport equations:

$$\frac{\partial \bar{u}_j k}{\partial x_j} = \frac{\partial}{\partial x_j} \left[\left(\frac{\nu_T}{\sigma_k} \right) \frac{\partial k}{\partial x_j} \right] + P_k - \varepsilon, \quad (9)$$

$$\frac{\partial \bar{u}_j \varepsilon}{\partial x_j} = \frac{\partial}{\partial x_j} \left[\left(\frac{\nu_T}{\sigma_\varepsilon} \right) \frac{\partial \varepsilon}{\partial x_j} \right] + \frac{\varepsilon}{k} (C_{\varepsilon 1} P_k - C_{\varepsilon 2} \varepsilon), \quad (10)$$

with P_k the production of TKE being defined as

$$P_k = -\overline{u'_i u'_j} \frac{\partial \bar{u}_i}{\partial x_j}. \quad (11)$$

These equations contain five closure constants; namely, C_μ , σ_k , σ_ε , $C_{\varepsilon 1}$, and $C_{\varepsilon 2}$. Different variants of the above model arise from the different approaches for determining the values for these coefficients. Here, four different high- Re $k-\varepsilon$ models are examined:

1. the standard (STD) $k-\varepsilon$ model [10];
2. the Kato–Launder (K–L) $k-\varepsilon$ model [11];
3. the renormalization group (RNG) $k-\varepsilon$ model [12];
4. the non-linear (N–L) eddy viscosity $k-\varepsilon$ model [13].

The first three models are based on the linear (Boussinesq) stress-strain relation. The model constants associated with the STD and K–L turbulence models are

$$C_\mu = 0.09, \quad \sigma_k = 1, \quad \sigma_\varepsilon = 1.3, \quad C_{\varepsilon 1} = 1.44, \quad C_{\varepsilon 2} = 1.92. \quad (12)$$

The major difference between the STD and K–L turbulence models lies in the modeling of the TKE production (P_k) term. Instead of using Eq. (11) as in the case of the STD model, which can be re-written as

$$P_k = C_\mu \varepsilon \tilde{S}^2, \quad (13)$$

for K–L model,

$$P_k = C_\mu \varepsilon \tilde{S} \tilde{\Omega}, \quad (14)$$

where

$$\tilde{\Omega} = \frac{\sqrt{2\Omega_{ij}\Omega_{ij}k}}{\varepsilon}, \quad \Omega_{ij} = \frac{1}{2} \left(\frac{\partial \bar{u}_i}{\partial x_j} - \frac{\partial \bar{u}_j}{\partial x_i} \right). \quad (15)$$

Here, $\tilde{\Omega}$ is the characteristic vorticity invariant that is constructed from the mean rotation tensor Ω_{ij} . The K–L turbulence model is designed specifically to suppress excessive turbulence energy production in stagnation regions. In particular, for simple shear flows $\tilde{S} \approx \tilde{\Omega}$ so predictions obtained from the K–L model are essentially identical to that of the standard model, while in a stagnation region $\tilde{\Omega} \approx 0$ so the

spurious turbulence energy production is eliminated here. For the RNG $k-\varepsilon$ model,

$$C_\mu = 0.085, \quad \sigma_k = 0.72, \quad \sigma_\varepsilon = 0.72, \\ C_{\varepsilon 1} = 1.44 - \frac{\tilde{S}(1 - \tilde{S}/4.38)}{1 + 0.012\tilde{S}^3}, \quad C_{\varepsilon 2} = 1.68. \quad (16)$$

Finally, for the N-L eddy viscosity model,

$$C_\mu = \frac{0.667}{1.25 + \tilde{S} + 0.9\tilde{\Omega}}, \quad \sigma_k = 1, \quad \sigma_\varepsilon = 1.3, \\ C_{\varepsilon 1} = 1.44, \quad C_{\varepsilon 2} = 1.92. \quad (17)$$

3.2. Numerical framework

Our computational domain for simulating the two-dimensional building array used in the wind tunnel experiment (cf. Fig. 1) extended in the streamwise direction from $x/H = -5$ to 28, with the upstream wall of the first building at $x/H = 0$. The height of the domain was $9H$. The results of the numerical simulation reported below were obtained with an orthogonal 251×51 grid shown in Fig. 1. The grid lines were concentrated near the solid surfaces (ground, rooftop, and building walls) and the spacing between grid lines was gently stretched at increasing distances from the solid surfaces.

Since the computational domain is chosen to be large compared with the two-dimensional array of obstacles, the flow at its boundary is not affected by any of the obstacles. Hence, free boundary conditions are imposed at all air-to-air boundaries in the flow domain. At the inflow boundary, the measured distributions of streamwise mean velocity, $\bar{u} \equiv \bar{u}_1$, the vertical mean velocity, $\bar{w} \equiv \bar{u}_3 = 0$, and the turbulence kinetic energy, k , are used. This information is obtained from the vertical profiles of \bar{u} and k measured furthest upstream from the upstream face of the first building (viz., at $x/H = -3.5$, or $x = -500$ mm, where $x = 0$ corresponds to the upstream wall of the first building). Above $z = 3H$, measurements for \bar{u} and k are not available; and, for the inflow boundary conditions, the vertical profile of \bar{u} above $z = 3H$ was assumed to adhere to a power-law profile described in Eq. (1), and the vertical profile of k was assumed to be constant above $z = 3H$ (corresponding, as such, to a deep constant stress layer). Unfortunately, at the inflow, ε was not measured and, consequently, was estimated simply as $\varepsilon = k^{3/2}/l$ where the dissipation length scale l was chosen as approximately $1.2H$. The length scale l is unknown at the inflow boundary, but variation of its value from $0.1H$ to $1.2H$ showed that it had only a very small impact on the final solution. Far downstream, at the outflow boundary, we set $\partial\bar{u}/\partial x = \partial k/\partial x = \partial\varepsilon/\partial x = \bar{w} = 0$. At the upper boundary, we set $\partial\bar{u}/\partial z = \bar{w} = 0$, $\partial k/\partial z = \partial\varepsilon/\partial z = 0$. Finally, at all solid boundaries (ground, obstacle walls, obstacle roofs) in the computational domain, standard wall functions are used for mean velocities and turbulence quantities [14].

The numerical method employs a structured, non-orthogonal (allowing boundary-fitted coordinates), fully colocated (viz., all flow variables are stored at the same

location), cell-centered, finite volume approach for the discretization of the computational domain. Within this non-orthogonal system, the velocity vector is decomposed into its Cartesian components, and these are the components to which the momentum equations relate. Advective volume face fluxes are approximated using a third-order upwind discretization scheme [15], and physical diffusive cell fluxes are approximated using a conventional second-order central differencing scheme. The SIMPLE algorithm [16] was used for pressure correction. Here, mass continuity is enforced by solving a pressure correction equation which, as part of the iterative sequence, steers the pressure toward a state at which all mass residuals in the cells are negligibly small. In conjunction with the colocated grid used here, this method is known to provoke checkerboard oscillations in the pressure field, reflecting a state of pressure–velocity decoupling. To avoid this, the widely used method of Rhie and Chow [17] is adopted to non-linearly interpolate the cell face velocities from the nodal values (at the center of the cells). The interpolation scheme essentially introduces a fourth-order pressure diffusion correction that smooths out the pressure if it oscillates rapidly. In the numerical scheme, the transport equations for the mean velocity, turbulence kinetic energy, and viscous dissipation rate and the pressure-correction equation are solved sequentially and iterated to convergence, defined by reference to the sum of the absolute cell residuals for mass and momentum components. A tri-diagonal matrix algorithm (TDMA) applied iteratively, in a line-by-line fashion, was utilized to solve the system of algebraic equations arising from the discretization of the transport equations and pressure-correction equation. Iterative refinement of all fields was continued until the sum of the absolute cell residuals for mass and for momentum was satisfied to within 0.1% of the total mass and momentum fluxes, respectively, at the inflow boundary. Further details of the numerical procedure can be found in Ref. [18].

3.3. Results and discussion

Figs. 2 and 3 show the mean flow streamlines superimposed on the turbulence kinetic energy field in the $x-z$ plane around and upstream of the first three buildings and around and downstream of the last building in the array, respectively, for the standard, K-L, RNG, and non-linear $k-\varepsilon$ turbulence models. Qualitatively, a number of gross features in the flow are correctly predicted by these models. The separation zone where the flow detaches from the windward rooftop edge of the first building and reattaches to the roof near the leeward rooftop edge, and the absence of such a separation zone on the subsequent (downwind) rooftops is well predicted, as is the single recirculating vortex that forms in the street canyon between the buildings. The stagnation point on the windward face of the first building which occurs at about one-half the building height is correctly predicted by the various models. The slow-moving and relatively large recirculation zone formed behind the leeward wall of the last building has been predicted, although two of the turbulence models (namely, the RNG and non-linear models) appear to overpredict and the other two models (namely, the standard and K-L models) appear to underpredict (albeit slightly) the experimental reattachment length ($\approx 3.8H$) of this separation

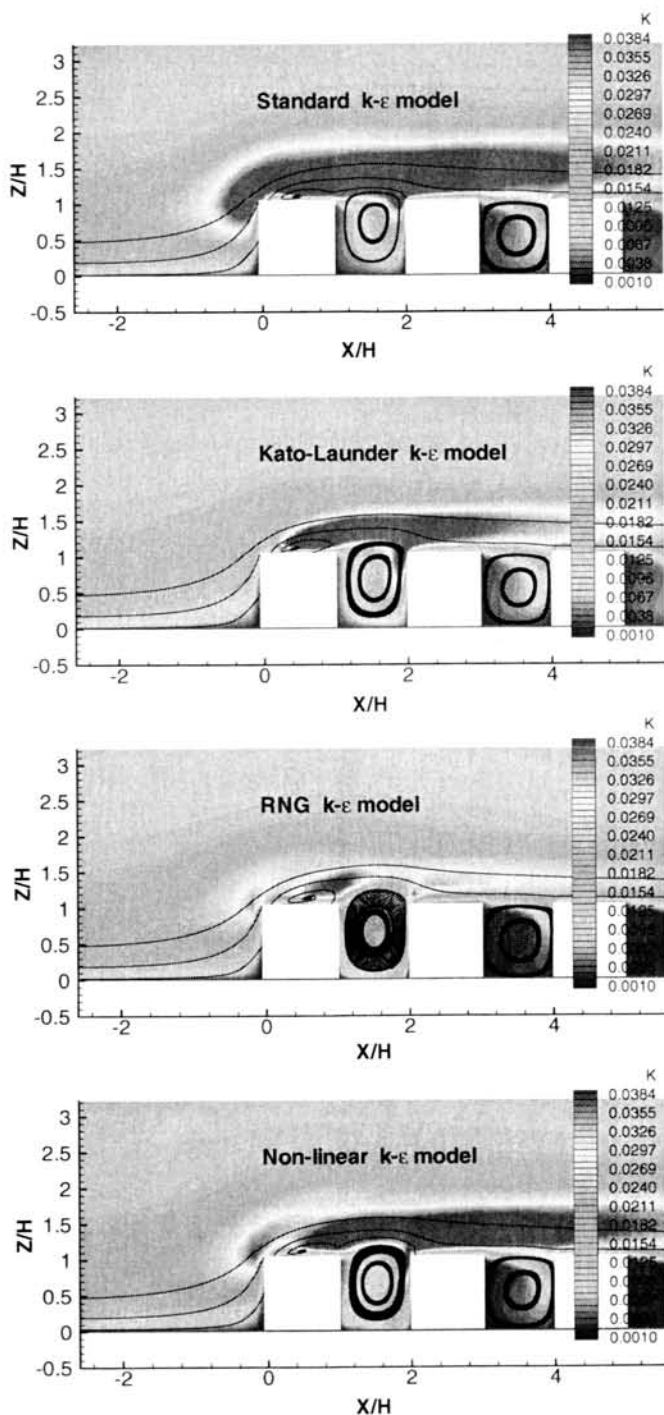


Fig. 2. Turbulence kinetic energy isopleths with the mean flow streamlines superimposed over the impingement zone and the first three buildings of the array.

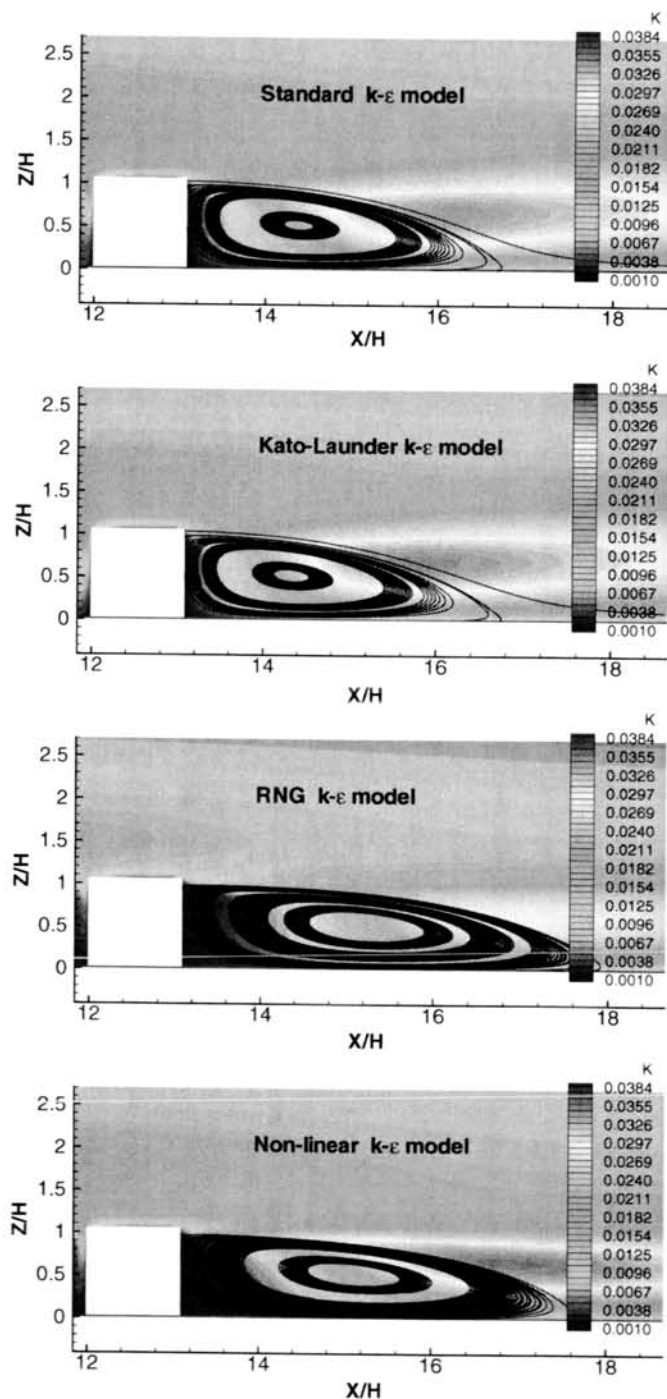


Fig. 3. Turbulence kinetic energy isopleths with the mean flow streamlines superimposed over the last building and the exit region of the array.

zone. All the turbulence models, with perhaps the exception of the K–L model (which was designed to solve the stagnation point anomaly by reducing the production of TKE in regions of high streamwise strain), exhibit a strong gradient of TKE centered near the top and slightly upstream of the windward edge of the rooftop of the first building with the TKE “exported” to locations downstream of this position in a broad TKE “plume”.

3.3.1. Mean streamwise velocity

Fig. 4 compares model predicted vertical profiles of the mean streamwise velocity \bar{u} at four fixed x -locations covering the range from within the impingement zone directly upstream of the first building, over the rooftop of the first building, into the first street canyon, and over the rooftop of the second building. At $x = -75$ mm, the wind speed reduction below and wind speed increase above the level $z/H \approx 4/3$ relative to the upstream profile is reproduced well. However, the models do not predict the reversal in the mean flow close to the ground at this position. Furthermore, close to the upstream wall of the first building at $x = -15$ mm (not shown), the significant wind speed reduction below the building height H owing to the adverse pressure rise (horizontal pressure gradient) upstream of the solid obstacle is modeled well, as is the moderate speed-up above the building rooftop. At $x = 75$ mm, the speed-up over the first rooftop compared with the reference upwind profile and the presence of a thin separation zone near the roof surface with flow reversal are well matched between the predictions and the measurements. The results for $x = 225$ mm show reasonable agreement between the measurements and the model predictions of \bar{u} in the first urban canyon. An important feature captured by the model predictions here is the very strong shear layer that forms immediately downstream of the rear face of the first building, whose signature is revealed by the inflection point in $\bar{u}(z)$ at or near the building height H . Note that the high values of mean shear $\partial\bar{u}/\partial z$ just above building height over the first urban canyon are reproduced well by the model. The speed-up above about $z/H \approx 4/3$ is predicted correctly over the first urban canyon, although the magnitude of the reverse flow in the canyon below about $z/H \approx 2/3$ is underestimated slightly by the standard $k-\epsilon$ model. The reverse velocity on the underside of the standing vortex within the canyon is comparable to the forward velocity at the canyon top, and this feature appears to be reproduced by the model predictions. Finally, the computed and measured mean streamwise velocity \bar{u} over the rooftop of the second building is well predicted. The models predicts that no separation occurs over the second rooftop (in contrast to the behavior over the first rooftop) which accords well with the observations.

Vertical profiles of \bar{u} at four x -locations within the second and third urban canyons and over the rooftops of the third and fourth buildings are displayed in Fig. 5. Note that the predicted magnitudes of the wind shear over the second and third street canyons are larger than what is observed in the wind tunnel measurements. The primary reason for this discrepancy appears to be the reduced vertical turbulent diffusion of shear stress in the high shear layer bordering the urban canyon top—a defect manifesting itself by the greater level of shear strain in this area

than observed. The reduced vertical turbulent diffusion results from the underestimation of the turbulence kinetic energy, which implies an underestimation in the turbulent viscosity. Because of this, the high shear layer generated near the urban canyon top dissipates more slowly in the streamwise direction along the canyon and the succeeding rooftops than in the wind tunnel observations. In consequence, the

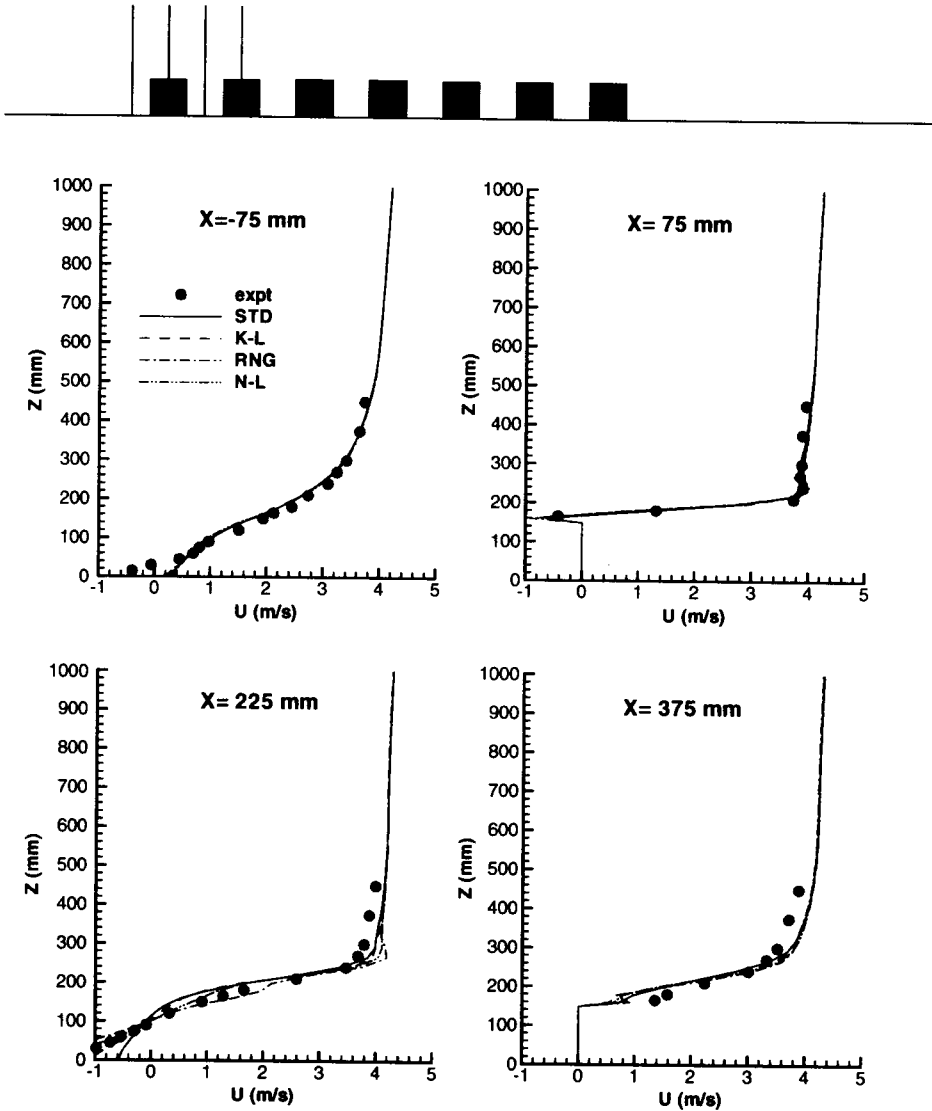


Fig. 4. Vertical profiles of the mean streamwise velocity \bar{u} at four x -locations ($x = -75, 75, 225$ and 375 mm), obtained from a high-resolution numerical simulation using four different turbulence models, are compared with time-averaged wind tunnel measurements at the same locations.

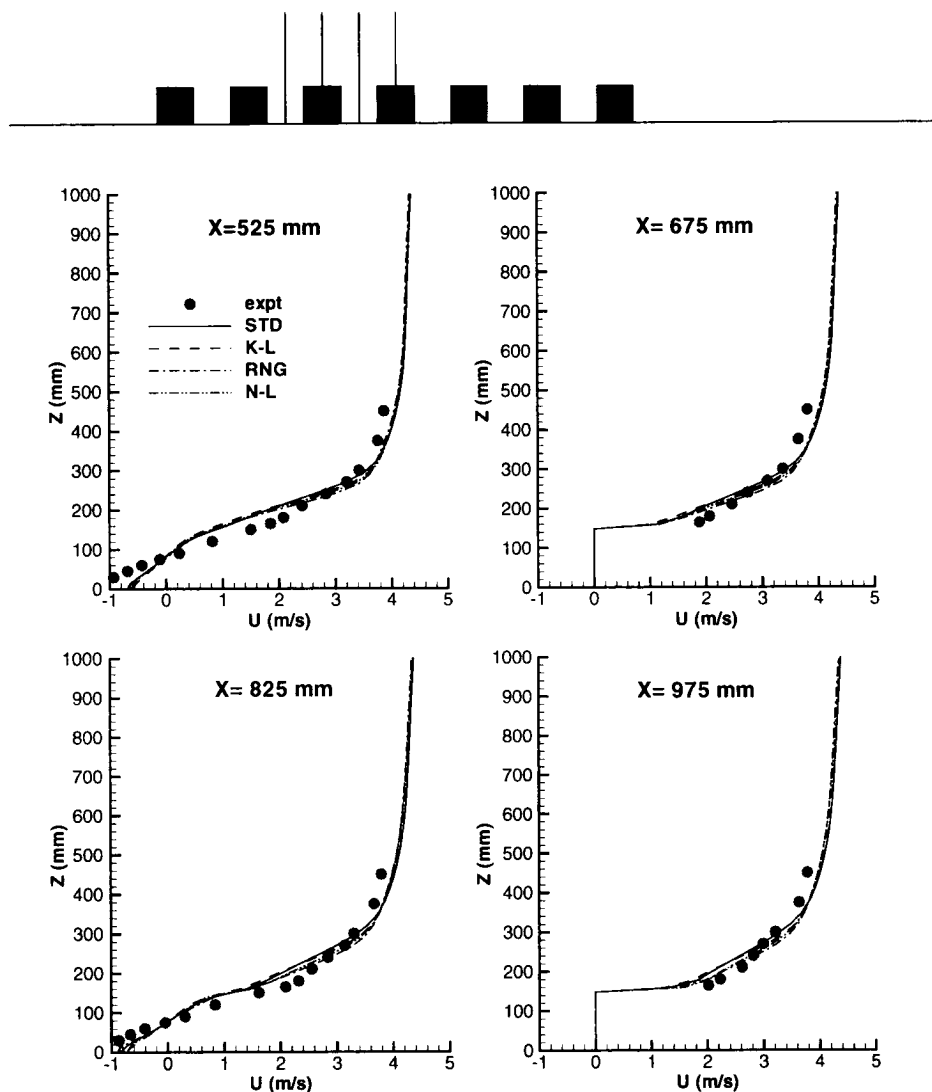


Fig. 5. Vertical profiles of the mean streamwise velocity \bar{u} at four x -locations ($x = 525, 675, 825$ and 975 mm), obtained from a high-resolution numerical simulation using four different turbulence models, are compared with time-averaged wind tunnel measurements at the same locations.

prediction of the speed-up above and wind reduction below the level $z/H \approx 4/3$ is slightly over-predicted and under-predicted, respectively.

Vertical profiles of both the computed and measured mean streamwise velocity \bar{u} within the third urban canyon and the fourth rooftop are almost identical to the profiles obtained, respectively, for the second urban canyon and the third rooftop. In consequence, \bar{u} appears to have reached streamwise equilibrium (i.e., the mean

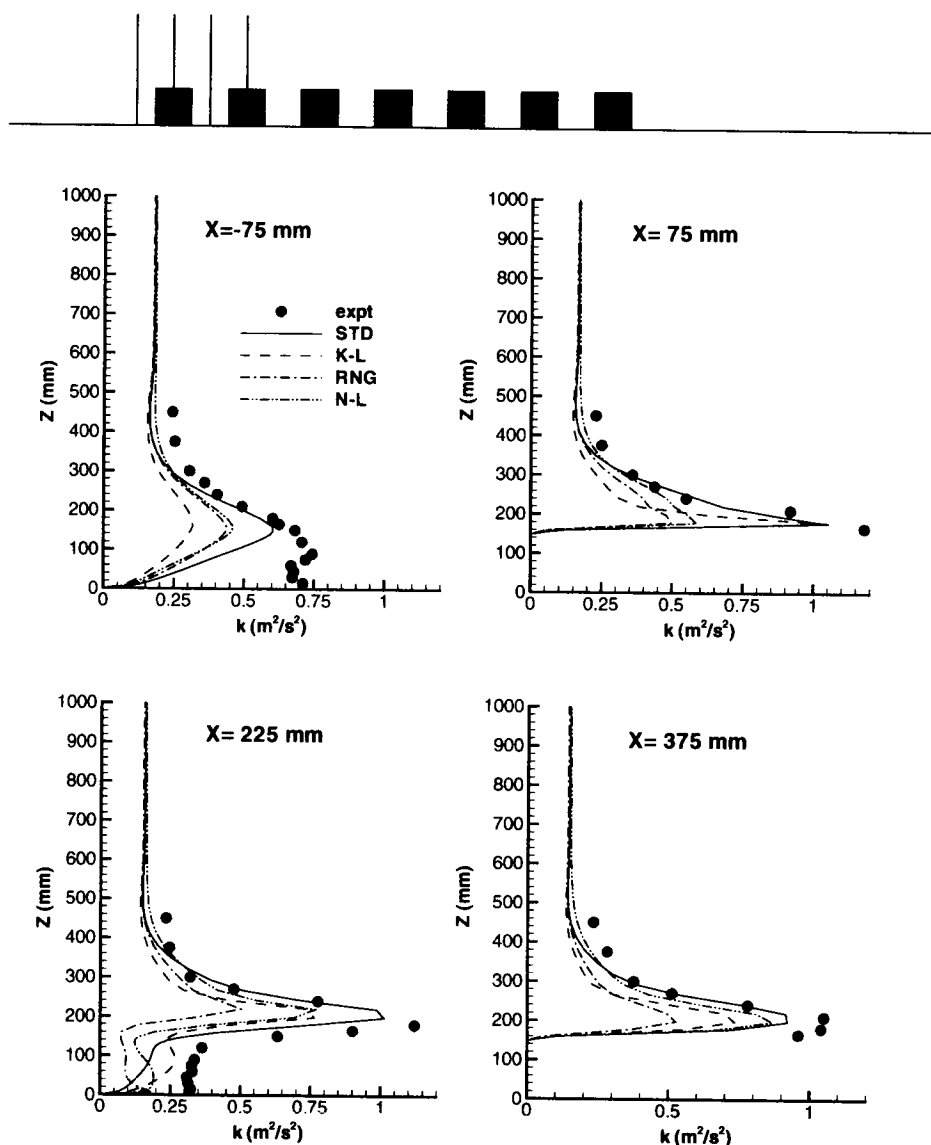


Fig. 7. Vertical profiles of the turbulence kinetic energy k at four x -locations ($x = -75, 75, 225$ and 375 mm), obtained from a high-resolution numerical simulation using four different turbulence models, are compared with time-averaged wind tunnel measurements at the same locations.

zone would correspond to a gain in $-\overline{u'w'}$ owing to the positive (unstable) flow curvature ($R > 0$) in this region (noting that $2\overline{u'^2} \gg \overline{w'^2}$). Hence, a reduction in normal-stress anisotropy would lead to an underestimation in $-\overline{u'w'}$, which in turn would lead to a reduced shear stress production, $-\overline{u'w'}\partial\bar{u}/\partial z$, of the TKE. Secondly,

an underestimation of the normal stress anisotropy will lead to an under-prediction of the normal stress production of k , $-(\overline{u'^2} - \overline{w'^2})\partial\bar{u}/\partial x$, in the impingement zone in front of the first building. Note that in this region $\partial\bar{u}/\partial x < 0$ owing to the deceleration of the flow in front of the windward face of the first building (induced by the adverse horizontal pressure gradient here), so the term (in streamline coordinate system) $-(\overline{u'^2} - \overline{w'^2})\partial\bar{u}/\partial x$, corresponds to a gain in TKE.

If we approximate $-(\overline{u'^2} - \overline{w'^2})\partial\bar{u}/\partial x$ by $4\nu_T(\partial\bar{u}/\partial x)^2$ following the Boussinesq linear stress-strain relation, then an excessive turbulence kinetic energy is expected to be generated along the stagnation line due to sufficiently high normal straining—a defect commonly referred to as the ‘stagnation point anomaly’. This results in the standard $k-\varepsilon$ model overestimating the TKE levels in the stagnation zone of a bluff body (see, for example, [14]). However, this seems to contradict the observed underestimation of the predicted levels of TKE in the impingement zone by the standard $k-\varepsilon$ model for the current situation. A possible explanation for this contradiction is that the standard $k-\varepsilon$ model does not account properly for the subtle effects of streamline curvature on the turbulence. In the present case, the impingement process occurring in front of the first building wall provokes a severe concave (unstable) flow curvature in the region of the flow immediately upstream of the first building rooftop. It is expected that the turbulence kinetic energy in this region will increase significantly due to the cumulative effect of concave streamline curvature as fluid elements are forced up and over the first building. The curvature term (in streamline coordinates) $-\bar{u}'w'(\bar{u}/R)$ is a source of production of k in this region of positive (unstable) R , and this source of TKE is not properly modeled in the standard $k-\varepsilon$ model.

Alternatively, the observed large peak in the TKE just above the first building rooftop can be also interpreted as arising from an oscillation of the high shear layer by the larger-scale upstream turbulence which would enhance \bar{u}'^2 (and, hence k). Certainly, this “flapping” of the shear layer at the building height over a street canyon has been reported in Ref. [19]. The fact that such a large peak is missing in the predictions may suggest that this process is not well represented in the $k-\varepsilon$ turbulence model. Indeed, steady RANS predictions cannot, of course, account for these large-scale unsteady motions (i.e., shear layer “flapping”). Since TKE is exported downstream by local advection and turbulent transport, an underestimation of the TKE level in the region just upstream of the first building will lead generally to an underestimation of the TKE level at all positions downstream of the location of strong turbulence generation, although this defect is expected to diminish with increasing downstream distance from the region of maximum TKE production.

The position of the prominent “nose” in the k profiles lying just above the street canyon top at $x = 225$ mm is largely reproduced by the numerical simulation (especially by the standard model), albeit the peak value of k is underestimated. This defect is a consequence of the under-prediction of the TKE level upstream of this region owing to the inability of the present models to account properly either for the effects of secondary strain on the turbulence and/or for the effects of the large-scale flapping of the strong shear layer at the canopy top. Moving downstream from this

position, the evolution of the TKE profiles is dominated by the vertical spreading of this shear or mixing layer (cf. Fig. 8). At the center of this layer lying just above the building height H , the peak value of TKE attenuates downstream. Turbulence energy is exported to regions below and above the peak by pressure or turbulent transport from the shear layer core, causing the TKE to increase in these regions.

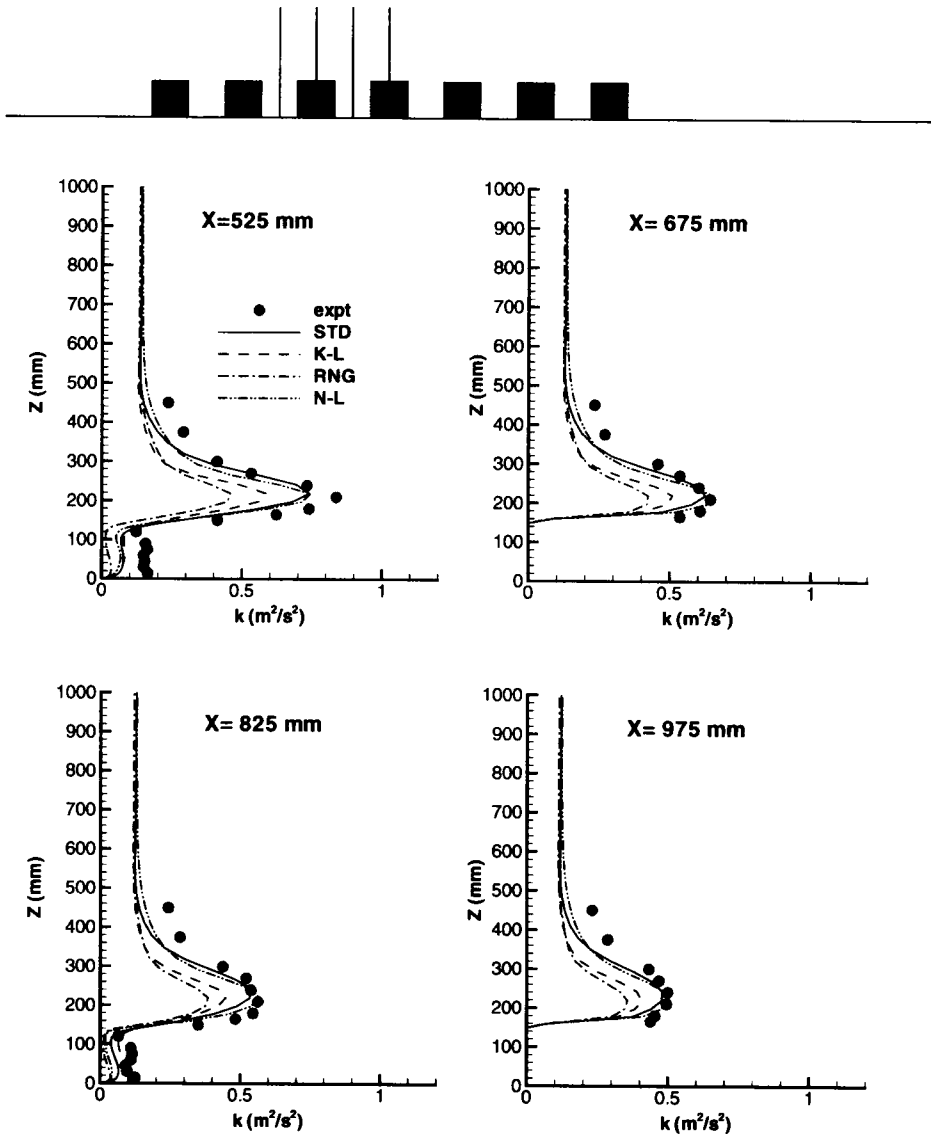


Fig. 8. Vertical profiles of the turbulence kinetic energy k at four x -locations ($x = 525, 675, 825$ and 975 mm), obtained from a high-resolution numerical simulation using four different turbulence models, are compared with time-averaged wind tunnel measurements at the same locations.

These characteristics of the flow are largely reproduced by the numerical simulations (especially by the standard and N-L turbulence models).

The downstream advection and vertical diffusion of TKE results in a larger level of turbulence energy being found on the downstream (leeward) side of a street canyon than the upstream (windward) side, a feature that is also present in the model predictions (not shown). Within the street canyon, minimum levels of TKE are found on the upstream side of the canyon (protected region) where the TKE is essentially independent of height. These features are reproduced in the simulations, although the near constant TKE level on the upstream side of the canyon is underestimated by the models. In addition, the TKE levels in street canyons further downstream are successively smaller owing to the fact that the peak TKE in the mixing layer above each canyon attenuates downstream (and, hence, there is less TKE available to transport into each successive street canyon downstream). These qualitative features of the flow are largely reproduced by the numerical simulations. The quantitative agreement between the computed and measured TKE profiles generally improves with increasing downstream distance. Finally, it appears that the rate of vertical spreading of the shear or mixing layer in the numerical simulation is smaller than in the measurements. This discrepancy may be the result of an underestimation of the turbulent viscosity ν_T owing to the smaller predicted TKE levels.

Fig. 9 compares computed and measured TKE profiles near the exit region of the array. Overall, the TKE profiles in the exit region appear to be very similar in shape, and all the qualitative features in these profiles appear to be correctly predicted; the quantitative agreement is also fairly good, except for the RNG model. For the profiles in the range from 2025 to 2775 mm (only profiles at $x = 2175$ and 2475 mm are shown here and both locations are within the recirculation zone), the position of the maximum TKE is fairly well predicted by all models. This position corresponds to the center of the curved shear layer that bounds or envelops the recirculation zone behind the last building. Finally, the rate of recovery of the TKE in the far wake region to the upstream reference condition is reproduced correctly. Even at $x = 3075$ mm or, equivalently, $x/H = 7.5$ downstream of the last building (measurement furthest downstream), the TKE profile has the appearance of a detached mixing layer despite the fact that the mean flow has re-attached at about $x/H = 3.8$ downstream of the last building (not shown). This profile form is a residue of the strong shear or mixing layer that detaches from the last building rooftop and spreads outward by pressure or turbulent diffusion until this vertically spreading mixing layer makes contact with the ground surface. This is an example of disequilibrium that results in the TKE profile at even the furthest downstream measurement position not having recovered to the reference far upstream state.

3.3.3. Summary of model performance

Based on the preceding results, it is found that

- (1) the non-linear $k-\varepsilon$ model is capable of overcoming the deficiency of the stagnation point anomaly associated with the standard $k-\varepsilon$ model and,

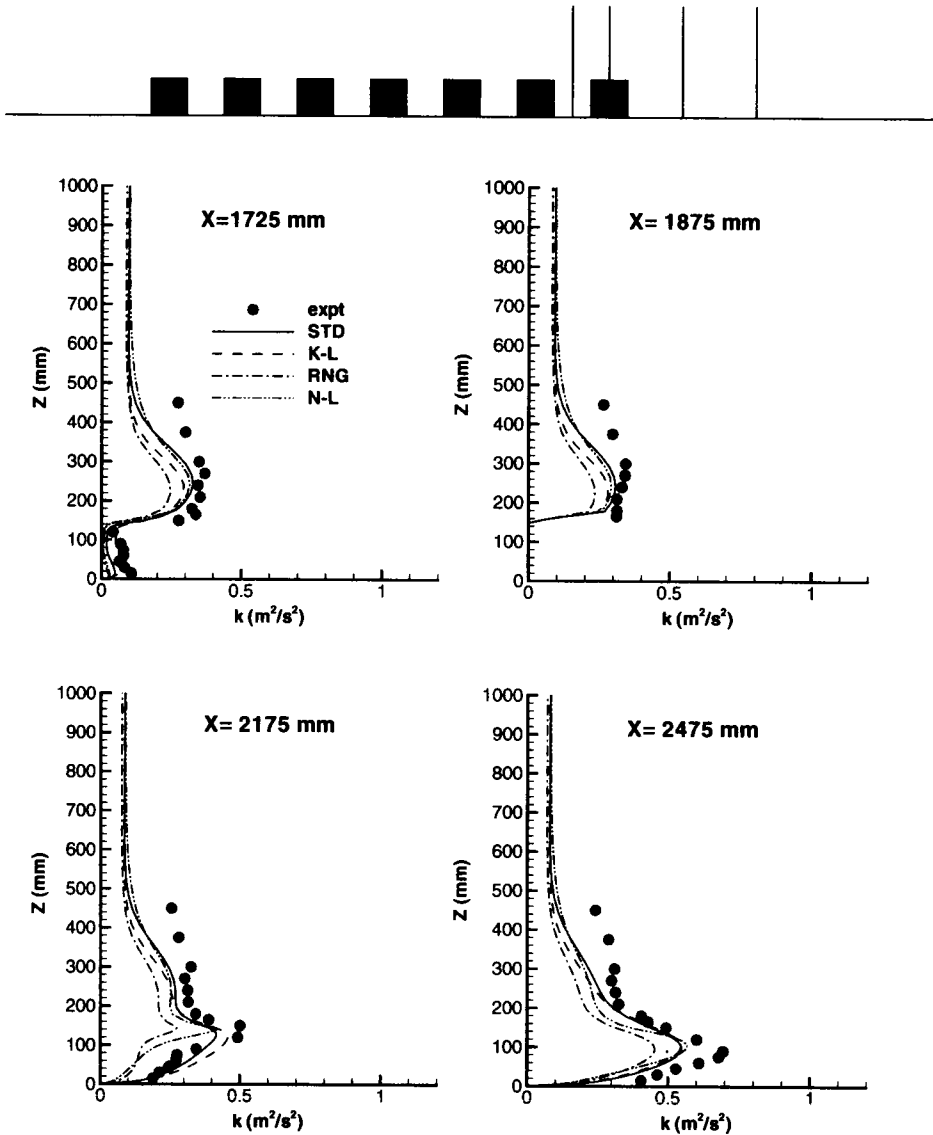


Fig. 9. Vertical profiles of the turbulence kinetic energy k at four x -locations ($x = 1725, 1875, 2175$ and 2475 mm), obtained from a high-resolution numerical simulation using four different turbulence models, are compared with time-averaged wind tunnel measurements at the same locations.

therefore, gives a better prediction of the mean streamwise velocity profile in the street canyon at $x = 225$ m (cf. Fig. 4);

- (2) the non-linear $k-\varepsilon$ model provides better predictions of the mean streamwise velocity profiles at $x = 2175$ and 2475 mm in the wake region behind the last

- building (cf. Fig. 6), especially above the canopy height, than the standard $k-\varepsilon$ and K-L turbulence models, although it overestimates the reattachment length;
- (3) the non-linear $k-\varepsilon$ model provides better predictions of the turbulence-energy profiles within the street canyon, above the rooftops of buildings, and in the wake region downstream of the last building compared to the RNG $k-\varepsilon$ model.

In addition, the non-linear $k-\varepsilon$ model is algorithmically simpler and numerically more robust and efficient than second-moment closure models. However, in many cases, the non-linear $k-\varepsilon$ model has a similar predictive performance compared with the (necessarily more complex) second-moment closure models [20,21]. Therefore, we recommend that the non-linear $k-\varepsilon$ model be used for the prediction of flows over a cluster of buildings.

4. Distributed drag force approach

4.1. Mathematical model

In the previous section, all the buildings in the array were resolved explicitly in the sense that boundary conditions were imposed at all the walls and roofs of the buildings. In this section, we will investigate the utility of representing individual buildings and/or groups of buildings in the obstacle array in terms of a distributed drag force. The process will involve the decomposition of the obstacle array into various contiguous regions that contain one or more obstacles with the aggregate effect of the obstacle(s) on flow in these regions represented by a drag coefficient. This approach will obviate the need to explicitly impose boundary conditions on the surfaces of all buildings (and other obstacles) in the array. A similar approach has been used by Belcher, Jerram, and Hunt [22] to study the adjustment of the mean velocity to a canopy of roughness elements using a linearized flow model (obtained by determining analytically small perturbations to the undisturbed upstream logarithmic mean velocity profile induced by the drag due to an obstacle canopy). However, this study investigated only the adjustment of the spatially averaged time-mean flow over a roughness element canopy, and did not focus on any of the turbulence statistics (e.g., turbulence kinetic energy).

The inclusion of additional source/sink terms in the mean momentum equations and the supporting k - and ε -equations to represent the aggregate effect of the obstacles on the flow can be obtained if we consider first the addition of an instantaneous (i.e., before the application of Reynolds averaging) drag force term

$$f_{Di} = C_D \hat{A} (u_i u_i)^{1/2} u_i, \quad (18)$$

which removes momentum in proportion to the instantaneous velocity, in the un-averaged Navier-Stokes equation. In Eq. (18), u_i is the instantaneous *spatially averaged* velocity, C_D is the drag coefficient, and \hat{A} is the frontal area density (i.e., the frontal area of the obstacles per unit volume of space). Now, using the Reynolds decomposition to decompose u_i into its mean \bar{u}_i and fluctuating u'_i components (viz.,

$u_i = \bar{u}_i + u'_i$), the instantaneous drag force can be expanded and then approximated up to third-order as follows:

$$\begin{aligned}
 f_{Di} &= C_D \hat{A} [(\bar{u}_j + u'_j)(\bar{u}_j + u'_j)]^{1/2} (\bar{u}_i + u'_i) \\
 &\approx C_D \hat{A} \left[(\bar{u}_j \bar{u}_j)^{1/2} + \frac{\bar{u}_j u'_j}{(\bar{u}_k \bar{u}_k)^{1/2}} \right] (\bar{u}_i + u'_i) \\
 &= C_D \hat{A} \left[\underbrace{(\bar{u}_j \bar{u}_j)^{1/2}}_I (\bar{u}_i + u'_i) + \underbrace{\frac{\bar{u}_j \bar{u}_i u'_j}{(\bar{u}_k \bar{u}_k)^{1/2}}}_{II} + \underbrace{\frac{\bar{u}_j u'_j u'_i}{(\bar{u}_k \bar{u}_k)^{1/2}}}_{III} \right]. \quad (19)
 \end{aligned}$$

In the second line of Eq. (19), it is assumed that $\bar{u}_j \bar{u}_j \gg u'_j u'_j$ and the binomial theorem is used to approximate the resulting square root term $(\bar{u}_j \bar{u}_j + 2\bar{u}_j u'_j)^{1/2}$.

The three terms (namely, I, II, and III) on the right-hand side of Eq. (19) correspond to various levels of approximation that have been applied to the expansion of the instantaneous drag force term in order to facilitate the subsequent Reynolds averaging process required to include this term in the mean momentum equations (and, also in the supporting transport equations for k and ε). For example, Getachew et al. [23] retain terms I, II, and III in their third-order approximation of the instantaneous drag force term. However, the treatment by Antohe and Lage [24] and Ayotte et al. [25] propose the retention of terms I and II only to give a second-order approximation for the instantaneous drag force term. Finally, Lee and Howell [28] use only term I in their first-order approximation of the instantaneous drag force term. We have used the drag parameter $C_D \hat{A}$ in our current parameterization of the instantaneous drag force term [cf. Eq. (18)], but in the porous media literature (e.g., Refs. [23,24]) this drag parameter is normally replaced by $F/\kappa^{1/2}$, where F is the Forchheimer constant (which has values approximately in the range from 0.075 to 0.5 according to measurements) and κ is the permeability. It is noted that $\kappa^{1/2}$ corresponds to a length scale that is characteristic of the effective pore size of the porous medium. Note that the dimension of $\kappa^{1/2}$ is the same as that of \hat{A}^{-1} (i.e., both are expressed in units of length). Hence, it is possible to make the following identification: $C_D \hat{A} \leftrightarrow F/\kappa^{1/2}$.

If we ensemble-average (or, time-average) the instantaneous drag force term of Eq. (19) with the retention of either terms I and/or II and ignore the 'dispersive stress' term¹ (see, for example, [25]) for simplicity (Ockham's razor), we find that the drag force contribution to the mean momentum equation (which is the prognostic

¹ The 'dispersive stress' corresponds to a 'dispersive' momentum flux term that physically arises from the correlations in the point-to-point variations in the time-averaged (mean) velocity field. Mathematically, this term arises from spatially averaging the non-linear convective term in the mean momentum (RANS) equation. The sparse experimental evidence to date seems to suggest that the dispersive stress term is negligible in comparison to the spatially averaged Reynolds stress [26] in a uniform plant canopy, but whether this is true for an urban-type roughness array remains to be demonstrated [27]. In a later section, we will use the high-resolution CFD results described in Section 3 to diagnose the dispersive stresses for 2D building array.

equation allowing the prediction of the spatially averaged time-mean velocity) has the following form:

$$\frac{\partial \bar{u}_i \bar{u}_j}{\partial x_j} = -\frac{1}{\rho} \frac{\partial \bar{p}}{\partial x_i} - \frac{\partial \overline{u'_i u'_j}}{\partial x_j} - \bar{f}_{D_i}, \quad (20)$$

where

$$\bar{f}_{D_i} = C_D \hat{A} (\bar{u}_j \bar{u}_j)^{1/2} \bar{u}_i \quad (21)$$

is the mean (ensemble-averaged) drag force exerted on a unit mass of fluid (or, specific drag force) in the x_i -direction induced by either a single canopy element or a group of canopy elements. In this section, unless otherwise noted, time and spatially averaged velocity components (subscripted) will be represented with overbars. Consequently, in Eq. (20), \bar{u}_i is interpreted as the spatially averaged time-mean velocity component in the x_i -direction within the context of the distributed drag force approach. Furthermore, in Eq. (20), it is noted that \bar{f}_{D_i} is defined to be positive in the direction opposite to \bar{u}_i (viz., the flow is decelerated if \bar{f}_{D_i} is positive; or, equivalently, the drag force always acts against the flow direction). The term \bar{f}_{D_i} represents the drag of the obstacles on the mean momentum. Finally, it is noted that a third-order approximation to the instantaneous drag force term results, on ensemble-averaging, in an additional term in the mean drag force involving the Reynolds stresses [23].

So far, we have considered only the addition of a mean drag force term \bar{f}_{D_i} to the mean momentum equation. The effect of form and viscous drag in the “urban” canopy on the k - and ε -equations will also require the inclusion of additional source and sink terms in these equations. It is remarked that in many simulations of canopy flow (or, of flow in porous media), no additional source and sink terms are included in the k - and ε -equations (e.g., Refs [29,30]), but as noted by Wilson [31] with reference to a second-order closure model the “quiet zone” corresponding to the region of reduced turbulence in the lee of a porous barrier cannot be properly simulated without the inclusion of an appropriate sink for u'^2 at the barrier. In view of this, we will adopt the idea of Lee and Howell [28] who proposed a simple treatment of source and sink terms in the k - ε turbulence model for the case of a highly porous layer exposed to a turbulent external flow field.

In the present study, we only consider Lee and Howell’s approach for simplicity. The other more complicated approaches (e.g., Refs [23,24]) lead to the addition of many more source/sink terms in the mean momentum and k - and ε -equations, but their accuracy and generality have not been proven; we prefer to retain the simplest model until the need for a better representation is demonstrated. In consequence, using the Lee and Howell [28] approximation for the instantaneous drag term [e.g., term I in Eq. (19)], the evolution equation for u'_i becomes

$$\frac{\partial u'_i}{\partial t} = \dots - C_D \hat{A} (\bar{u}_j \bar{u}_j)^{1/2} u'_i. \quad (22)$$

Multiplying Eq. (22) by u'_i , applying the summation in i , averaging in time (Reynolds averaging), and using the definition $k \equiv \overline{u'_i u'_i} / 2$ yields the evolution

equation for the (spatially averaged) TKE:

$$\frac{\partial k}{\partial t} = \dots \underbrace{-2C_D \hat{A}(\bar{u}_j \bar{u}_j)^{1/2} k}_{\text{extra sink term due to drag}} \quad (23)$$

In view of this, the evolution equation for k can be written explicitly as

$$\frac{\partial \bar{u}_j k}{\partial x_j} = \frac{\partial}{\partial x_j} \left[\left(\frac{v_T}{\sigma_k} \right) \frac{\partial k}{\partial x_j} \right] + (P_k - \varepsilon) - 2C_D \hat{A}(\bar{u}_j \bar{u}_j)^{1/2} k. \quad (24)$$

The extra sink term in the transport equation for k represents the loss from k to smaller scales and physically corresponds to the loss of energy from the turbulent eddies in the canopy as these eddies do work against the form and viscous drag of the canopy elements. The modeled transport equation for ε cannot be derived systematically. However, a dimensionally consistent analogy to the above k -equation can be written down as a modeled evolution equation for ε :

$$\frac{\partial \bar{u}_j \varepsilon}{\partial x_j} = \frac{\partial}{\partial x_j} \left[\left(\frac{v_T}{\sigma_\varepsilon} \right) \frac{\partial \varepsilon}{\partial x_j} \right] + \frac{\varepsilon}{k} (C_{\varepsilon 1} P_k - C_{\varepsilon 2} \varepsilon) - 2C_D \hat{A}(\bar{u}_j \bar{u}_j)^{1/2} \varepsilon. \quad (25)$$

4.2. Determination of the drag coefficient

The approach for parameterizing the mean drag force in terms of C_D , described in Section 4.1, has been applied previously to the numerical modeling of flows in both vegetative (e.g., Refs. [25,32–36]; among others) and urban (e.g., Refs. [37–39]) canopies. A major problem with this approach resides in the assignment of an appropriate value for C_D for a canopy consisting of an arbitrary geometrical arrangement of elements. This is a non-trivial and unsolved problem for there is currently no general method that can be used to predict the in situ drag coefficient of an element within a canopy from a knowledge of the drag coefficient of the element in isolation and the geometrical arrangement of the elements within the canopy.

In view of this difficulty, the drag coefficient C_D has usually been treated as an adjustable model parameter whose value is chosen to optimize the fit between the predicted and measured mean velocity profiles (e.g., Refs. [25,33]). Alternatively, for horizontally homogeneous canopies with no mean horizontal pressure gradient, either a local or bulk drag coefficient for the canopy can be diagnosed from the measured (observed) profiles of shear stress and mean velocity [40].

For a horizontally homogeneous canopy with no appreciable streamwise mean pressure gradient (i.e., for fully developed flow), the mean momentum equation within the canopy simply involves a balance between the stress gradient force (i.e., the vertical gradient of the shear stress) and the drag force (imposed on the flow by the canopy). Hence, the measured $\bar{u}(z)$ and kinematic shear stress $\hat{\tau}(z) \equiv -\overline{u'w'}$ can be used to diagnose the local drag coefficient parameter as

$$C_D \hat{A}(z) = - \left(\frac{\partial \overline{u'w'}}{\partial z} \right) / \bar{u}^2. \quad (26)$$

If vertical profiles of the shear stress are not available, a bulk drag coefficient parameter $C_D \hat{A}$ (which is assumed to be constant with height) can be determined as follows:

$$\hat{\tau}(H) = C_D \hat{A} \int_0^H \bar{u}^2 dz, \quad (27)$$

where $\hat{\tau}(H)$ is the kinematic shear stress at the canopy top (i.e., at $z = H$ where H is the canopy height). Eq. (27) is obtained by integrating Eq. (26) with respect to z from ground level to the canopy top and assuming that the shear stress vanishes at the ground (viz., $\hat{\tau}(z = 0) = 0$; or, equivalently, that the momentum absorbed by the ground is negligible compared to that absorbed by the canopy). The value of $C_D \hat{A}$ determined from either Eqs. (26) or (27) can then be used in a numerical model to predict the canopy flow. However, given the assumptions used to derive either Eqs. (26) or (27), this approach is not applicable for developing and/or horizontally inhomogeneous canopy flows. We require an alternative methodology for the determination of C_D in this case.

The drag force F_D , exerted on a canopy element or group of canopy elements in a control (averaging) volume V in the x_i -direction is the surface integral of the pressure (form) and viscous (frictional) forces over all canopy element surfaces contained in V [25]; namely,

$$F_{D_i} = \int_S (n_i \bar{p} - n_j \tau_{ji}) dS, \quad (28)$$

where n_i is the unit normal vector in the x_i -direction pointing away from the surface of the canopy element into the fluid, and τ_{ji} is the dynamic shear stress in the x_i -direction exerted on a surface (plane) of a canopy element perpendicular to the x_j -direction. Here, the shear stress τ_{ji} on the surface of a canopy element will be obtained explicitly from a high-resolution CFD simulation using the ‘wall-function’ approach (e.g., Ref. [14]). Once the drag force F_D has been determined, a drag coefficient C_D can be diagnosed using this information.

In this paper, we will explicitly diagnose a drag coefficient C_D for the case of a developing flow over an array of 2D obstacles using high-resolution CFD. More specifically, the test problem here is the same as in Section 3.3—namely, a developing flow over an array of seven 2D buildings. In this case, C_D must necessarily account for the effects of the drag on the “urban” canopy turbulence and the ‘sheltering’ within the canopy. In consequence, C_D does not necessarily have to be constant for each building in this array. Specifically, it is anticipated that the form (pressure) drag will be large for the first and/or second buildings of the array in the upstream direction where the incident flow first impinges on the array. To proceed with the analysis, we decompose the 2D building array into six “drag units” as illustrated in Fig. 10(a). Each drag unit consists of one building and the associated downstream street canyon. The seventh building in the array will be explicitly resolved (i.e., appropriate boundary conditions will be imposed along the walls and rooftop of this last building).

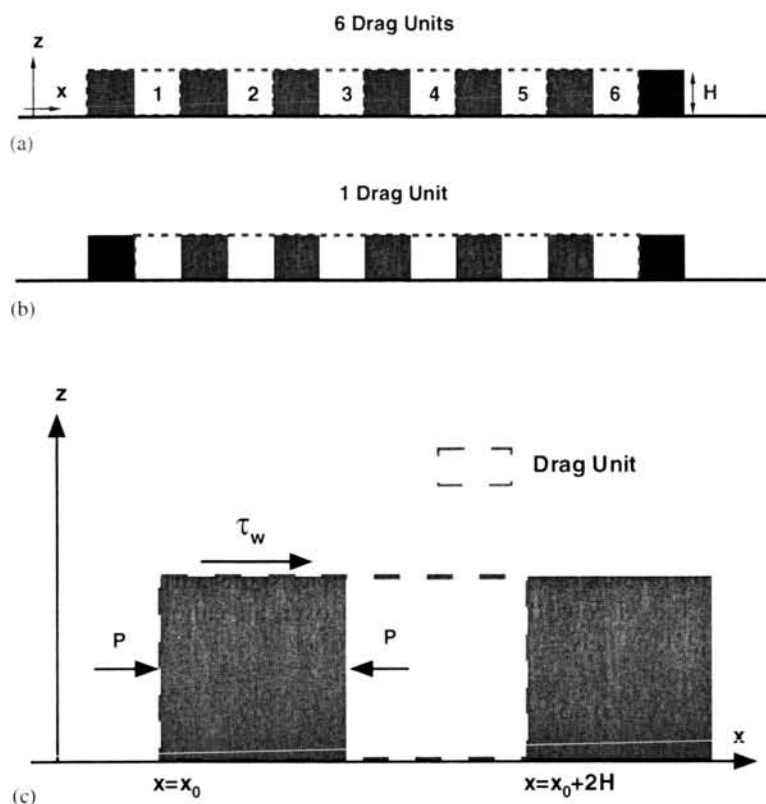


Fig. 10. Decomposition of the array into (a) six drag units with the last obstacle of the array explicitly resolved; (b) one drag unit with the first and last obstacles of the array explicitly resolved; and, (c) expanded view of one drag unit from (a) showing the "forces" acting on the surface of the drag unit.

Now, consider the expanded view of one of these drag units shown in Fig. 10(c). The control volume occupied by the drag unit is assumed to have unit length in the spanwise (or, y -) direction. The balance of force (or, equivalently, force per unit spanwise length) in the streamwise (or x -) direction for the control volume can be written as [cf. Eq. (28)]

$$F_{Dx} = \left[\int_{z=0}^{z=H} (\bar{p}|_{x=x_0} - \bar{p}|_{x=x_0+H}) dz + \int_{x=x_0}^{x=x_0+H} (\tau_w|_{z=H}) dx \right], \quad (29)$$

where τ_w is the wall shear stress in the x -direction exerted on the surface of the building in the z - (or, vertical-) direction. The first term in Eq. (29) is the contribution to the drag force resulting from the pressure discontinuity across the solid obstacle in the control volume and the second term is the contribution arising from the frictional force along the surface of the building(s) in the control volume.

The drag force F_{Dx} enables a bulk drag coefficient to be defined as follows:

$$C_D \equiv \frac{|F_{Dx}|}{\rho \int_{z=0}^{z=H} \langle \bar{u} \rangle^2(z) dz}, \quad (30)$$

where

$$\langle \bar{u} \rangle(z) = \frac{1}{2H} \int_{x=x_0}^{x=x_0+2H} \bar{u}(x, z) dx. \quad (31)$$

Furthermore, with the understanding that the drag force always acts against the direction of the flow, we have used the absolute value of F_{Dx} (i.e., magnitude of the drag force F_{Dx}) in the definition of C_D to ensure that C_D is always positive definite. For simplicity, the diagnosis of C_D (from a high-resolution CFD) using the definition in Eq. (30) with the drag unit decomposition for the obstacle array shown in Fig. 10(a) will be referred to henceforth as Method (a).

The values of C_D for each drag unit in Fig. 10(a) obtained using Method (a) are shown in Fig. 11(a). Here, the drag coefficient is presented in the form of a non-dimensional drag parameter $C_D A H / V$, where the frontal area A of the drag unit per unit spanwise length is $A = H$ and the volume V of the drag unit per unit spanwise length is $V = 2H^2$, so $\hat{A} = A/V = (2H)^{-1}$. These results demonstrate explicitly that the drag coefficients C_D of the first two drag units on the upstream side of the array are significantly larger than C_D of the remaining four drag units on the downstream side of the array. The reduction of the drag coefficient for the drag units “deep” within the array may be an example of the ‘shelter effect’ [41] arising from the mutual interference of the canopy elements.

We are interested also in the determination of the in-situ drag coefficient C_D of a drag unit within the 2D obstacle array where the flow becomes fully developed (viz., in the region of the array where there is negligible streamwise development of the flow statistics). In order to determine C_D for the streamwise equilibrium (fully developed) condition in the array, we extended the streamwise extent of the array to include 14 2D obstacles (or, 13 drag units). Results for C_D from the high-resolution numerical simulation for this case are displayed in Fig. 11(b). These results imply that the in situ drag coefficient $C_D \hat{A} H$ (or, equivalently, $C_D A H / V$) for a canopy element within the array in the regime of streamwise equilibrium is about 1.67.

The major disadvantage of the drag force representation exhibited in Fig. 10(a) is that a drag unit is associated with each obstacle in the array and the drag coefficient for each of these drag units is required as input information, with the drag coefficients determined from a numerically expensive high-resolution CFD simulation. The computational cost increases as the number of obstacles in the array increases. One may argue that, if a high-resolution CFD simulation is already available, there is no need for the drag force approach. Fortunately, in practice, it is not necessary to associate a drag unit with every single obstacle in the array because C_D approaches its fully developed value within the array relatively quickly as shown in Fig. 11(b), although C_D here appears to deviate slightly from its fully developed value again for drag units 12 and 13 on the downstream end of the array. This is due to the pressure effect arising from the wake downstream of the last obstacle (i.e., the

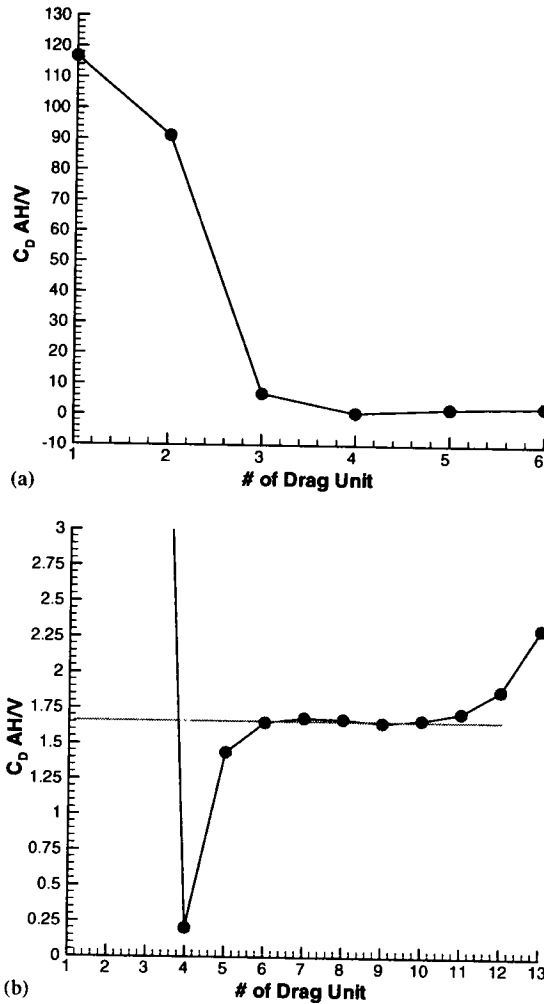


Fig. 11. The variation of the non-dimensional drag parameter $C_D AH/V$ for (a) decomposition of the original array into six drag units and (b) decomposition of an extended array into thirteen drag units.

14th obstacle of the array) propagating upstream. The results of Fig. 11(b) provide the motivation for the development of an alternative method for the representation of 2D array of obstacles by the drag force approach as illustrated in Fig. 10(b). Here, the first and last obstacles of the array are resolved explicitly, whereas all the intervening obstacles between the first and last obstacles are represented using one drag unit of length $11H$ and height H . The drag parameter $C_D \hat{A}H$ for this single unit is taken to be the in situ drag coefficient in the regime of streamwise equilibrium within the (extended) array. The drag representation of the building array shown in Fig. 10(b) with the single drag unit assigned the drag parameter $C_D \hat{A}H = 1.67$ will be referred to as Method (b) henceforth.

4.3. Results and discussion

Because the representation of obstacles using a distributed drag force approach in the flow model “smears” out the local heterogeneity of the detailed flow field in an obstacle array, it is convenient (and, perhaps, more appropriate) to compare the predictions of mean flow and turbulence from these models with spatially averaged flow quantities. As an example of these flow quantities, Figs. 12(a) and (b) show, respectively, vertical profiles of observed mean streamwise velocity \bar{u} and turbulence kinetic energy k at 10 x -positions within drag unit 4 [cf. Fig. 10(a)] along with the horizontally averaged mean velocity and turbulence kinetic energy profiles within the drag unit (which are obtained by averaging at each height z , $\bar{u}(x, z)$ and $k(x, z)$ over the 10 x -locations within the drag unit). The 10 x -locations shown in Fig. 12 correspond to 5 positions over the rooftop of the fourth building [$x \in (900, 1050)$ mm] and 5 positions over the fourth street canyon [$x \in (1050, 1200)$ mm] of the array.

The local heterogeneity of the mean flow and turbulence energy over drag unit 4 is clearly seen in Fig. 12. It is noted that the horizontal heterogeneity of k is stronger than that of \bar{u} . In particular, profiles of k below the building height at $z = H = 150$ mm near the lee side of the street canyon give substantially higher values of the TKE than locations within the protected zone near the windward side of the canyon. Unless otherwise indicated, all the simulations using the distributed drag force approach shown here are based on modifications of the K-L $k-\varepsilon$

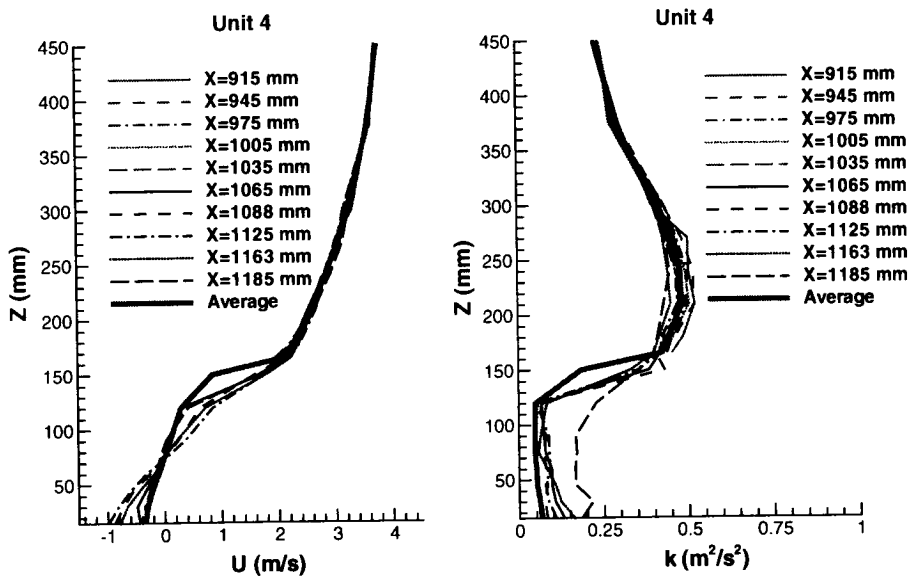


Fig. 12. Profiles of the mean streamwise velocity \bar{u} and turbulence kinetic energy k measured at 10 x -locations within drag unit 4 (i.e., over the fourth building rooftop and the fourth street canyon of the array). The horizontally averaged mean streamwise velocity and turbulence kinetic energy over the drag unit are also displayed.

turbulence model (by the inclusion of additional source/sink terms in the k - and ε -equations as described in Section 4.1).

Fig. 13 exhibits the modeled and measured mean streamwise velocity and turbulence kinetic energy obtained with the distributed drag force approach at $x = 225$ mm (i.e., at the center location of the first street canyon). At this location, note that the horizontally averaged mean streamwise velocity observed experimentally and predicted using a high-resolution CFD simulation (denoted, respectively, as Expt-ave. and HR-ave. in Fig. 13) are in very good agreement. The modeled mean velocity profiles obtained by Method (a) differs from the observed values (represented by the filled circles in Fig. 13) by 20% or less within the roughness sublayer ($1 \lesssim z/H \lesssim 2$), with the greatest discrepancy below the building height $z = H = 150$ mm where the modeled mean flow velocities are seen to under-predict the magnitude of the observed mean flow reversal near the ground. Furthermore, the modeled mean velocity profiles exhibit the greatest shear near the top of the obstacle array, with greatly reduced shear within the “urban” canopy which accords well with the observations. Finally, the modeled mean velocity profiles obtained using Method (b) (i.e., one drag unit) provides slightly poorer predictions for \bar{u} .

Because the turbulence energy levels are underestimated by the high-resolution CFD simulations, it is not surprising that the horizontally averaged TKE obtained using the high-resolution CFD also underestimates the experimentally observed horizontally averaged TKE (cf. Fig. 13). Interestingly, the prediction of the

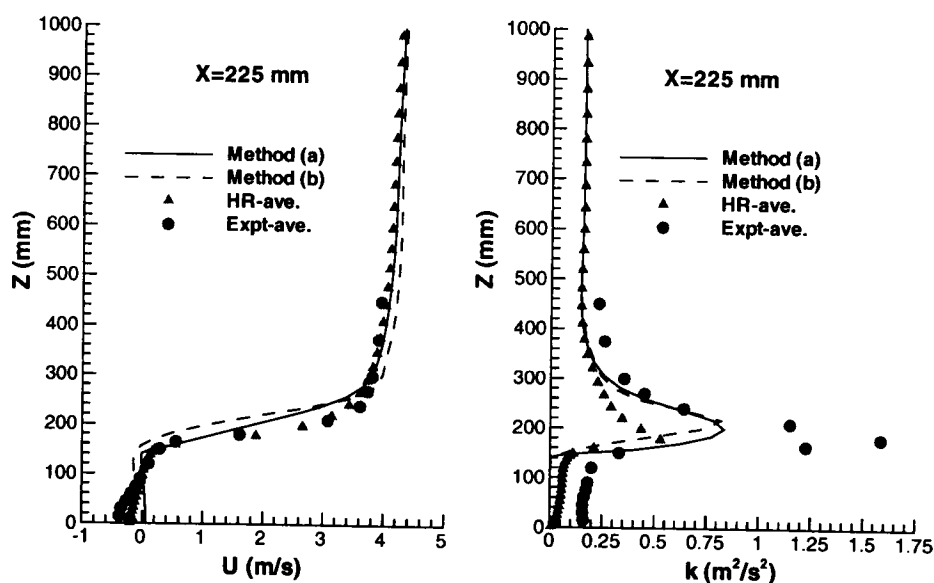


Fig. 13. Mean streamwise velocity \bar{u} and turbulence kinetic energy k profiles predicted using the distributed drag force approach at position $x = 225$ mm (center of the first street canyon) are compared with observed values (Expt-ave.) and high-resolution numerical simulation predictions (HR-ave.) of the horizontally averaged \bar{u} and k .

horizontally averaged TKE using the distributed drag force approach is better than that obtained by using the high-resolution CFD simulation (the latter of which is obtained by averaging the local TKE vertical profiles over the first drag unit). Again, it is noted that the modeled TKE profile obtained using Method (b) provides a slightly poorer prediction than that obtained using Method (a). Nevertheless, the simulated TKE for both methods is largest within the roughness sublayer at $z/H \approx 4/3$, and is reduced significantly within the “urban” canopy layer, in good agreement with the observations.

Figs. 14 and 15 compare the mean streamwise velocity and turbulence kinetic energy simulated using the distributed drag force approach with the observed values at single locations $x = 525$ mm (center of the second street canyon) and $x = 1125$ mm (center of the fourth street canyon), respectively. The mean velocity profile at $x = 525$ mm for Method (a) is in very good agreement with the experimental results, with the result from Method (b) giving only slightly poorer agreement in this case. The TKE profiles predicted with Methods (a) and (b) at $x = 525$ mm agree quite well with the measured profiles, with an under-prediction of the turbulence energy levels at $z/H \approx 4/3$ by about 20% at most. In contrast, at $x = 1125$ mm, the strong shear in the mean velocity profile near the canopy top at $z = H$ is under-predicted, whereas the turbulence energy levels within the urban canopy ($0 \leq z/H \leq 1$) and the roughness sublayer ($1 \leq z/H \leq 2$) are over-predicted (the more so within the urban canopy layer) by both methods.

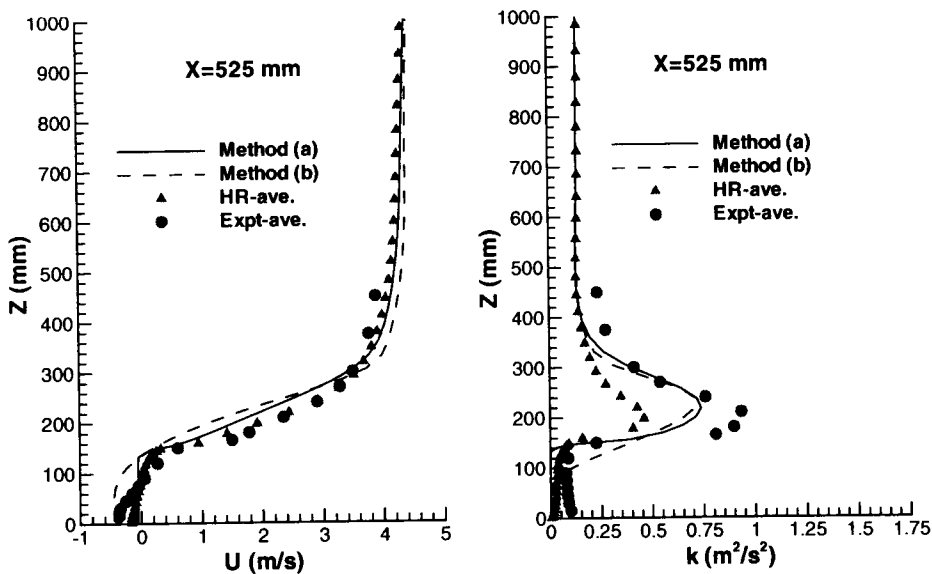


Fig. 14. Mean streamwise velocity \bar{u} and turbulence kinetic energy k profiles predicted using the distributed drag force approach at position $x = 525$ mm (center of the second street canyon) are compared with observed values (Expt-ave.) and high-resolution numerical simulation predictions (HR-ave.) of the horizontally averaged \bar{u} and k .

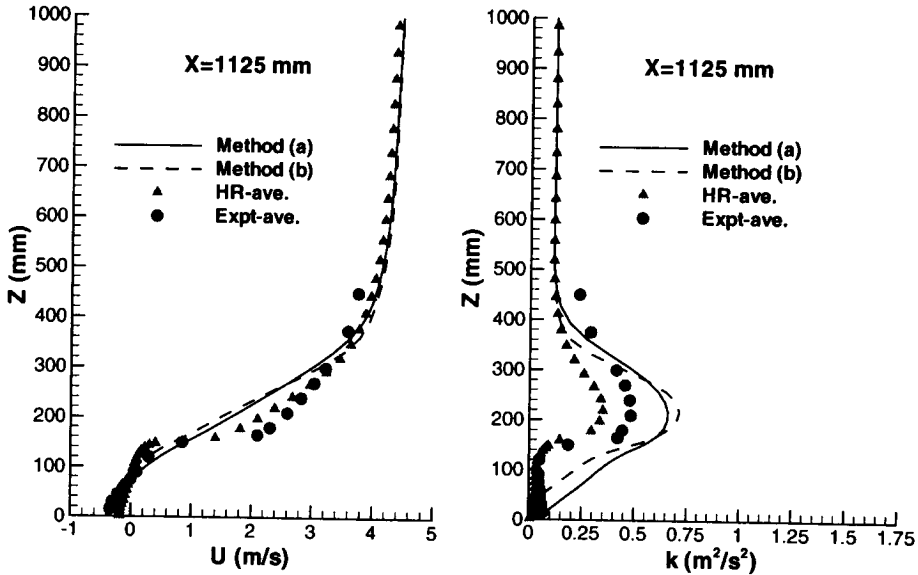


Fig. 15. Mean streamwise velocity \bar{u} and turbulence kinetic energy k profiles predicted using the distributed drag force approach at position $x = 1125$ mm (center of the fourth street canyon) are compared with observed values (Expt-ave.) and high-resolution numerical simulation predictions (HR-ave.) of the horizontally averaged \bar{u} and k .

The simulated and observed mean streamwise velocity and turbulence kinetic energy at $x = 1425$ mm (center of the fifth street canyon) are compared in Fig. 16. As for the case at $x = 1125$ mm (cf. Fig. 15), the magnitude of the mean wind shear at or near $z = H$ is under-predicted by both methods. However, note that the magnitude of the mean velocity at positions within the canopy ($z/H \lesssim 2/3$) is in good conformance with the experimental results. Note that as one progresses “deeper” into the obstacle array, the differences in the mean velocity predicted by Methods (a) and (b) become smaller (as the mean flow converges towards the condition of streamwise equilibrium within the array). Even so, the condition of *exact* streamwise equilibrium for the spatially averaged time-mean flow within the canopy has not been achieved even by row 6 of the array. In particular, note from Fig. 16 that the spatially averaged time-mean flow is slightly negative below about $z/H \lesssim 1/4$, which agrees with the reverse flow observed here in the spatially averaged experimental data (Expt-ave) and predicted by the spatially averaged high-resolution CFD results (HR-ave) for the mean velocity. In the dense 2D building array studied here, the vertical momentum flux resulting from the turbulent stresses do not penetrate very deeply into the urban canopy [in particular, note from Fig. 19 that turbulent shear stress divergence is approximately zero near the base of 2D building array ($0 \lesssim z/H \lesssim 1/2$)], so the flow here is effectively vertically decoupled from the flow aloft. Deep within the urban canopy, the spatially averaged time-mean momentum budget reduces to a balance between the streamwise advection on the one hand and

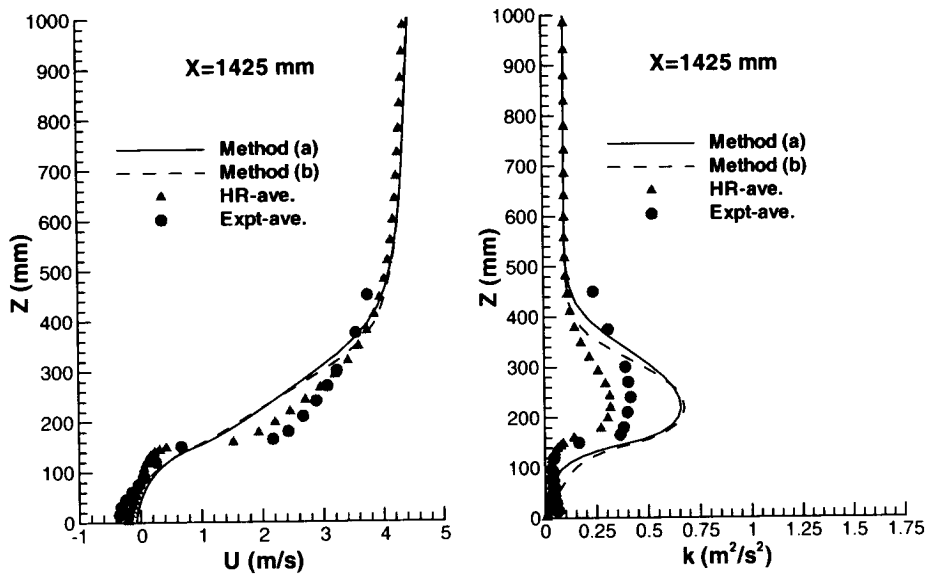


Fig. 16. Mean streamwise velocity \bar{u} and turbulence kinetic energy k profiles predicted using the distributed drag force approach at position $x = 1425$ mm (center of the fifth street canyon) are compared with observed values (Expt-ave.) and high-resolution numerical simulation predictions (HR-ave.) of the horizontally averaged \bar{u} and k .

the pressure gradient and canopy drag on the other hand. At row 6 of the array, the pressure gradient term in the streamwise spatially averaged momentum transport equation is small, but not exactly zero (implying that the condition of streamwise equilibrium here is not exact). This adverse pressure gradient force, though small within the canopy, is nevertheless large enough to cause a small reverse velocity deep within the canopy ($z/H \lesssim 1/4$) (viz., the magnitude of the spatially averaged time-mean flow tends to be small there, so even a very weak adverse pressure gradient force can result in a back flow there).

Note that the spatially averaged time-mean velocity \bar{u} obtained with the distributed drag force model underpredicts \bar{u} in relation to both the HR-ave and Expt-ave (cf. Fig. 16) above the canopy. In addition, the shape of \bar{u} obtained from the distributed drag force approach is different than that exhibited by both HR-ave and Expt-ave for $4/3 \lesssim z/H \lesssim 7/3$ (corresponding roughly to the inertial sublayer). The mean flow shown in Fig. 16 can be used to diagnose a roughness length z_0 for 2D building array, which in this case, corresponds to a skimming flow over the array. Fitting \bar{u} in the inertial sublayer to a standard semi-logarithmic mean velocity profile, the following values of z_0 were inferred: $z_0/H \approx 0.0085$ for Expt-ave; $z_0/H \approx 0.0095$ for HR-ave; and $z_0/H \approx 0.15$ for Method (a) and Method (b) (which are obtained from the distributed drag force approach). Note that for the case of skimming flow over a 2D array of buildings, the distributed drag force approach gave a poor estimate for z_0 . However, the mean flow obtained by spatially averaging the

high-resolution CFD results yields a value for z_0 that agrees well with the measured value of z_0 (the latter obtained from the spatially averaged experimental data for the mean velocity). The value of z_0 diagnosed here for the 2D building array from the experimental data appears to be larger than a roughness length of $z_0/H \approx 0.001$ obtained for a square bar array (cf. Fig. 2 in [42]) with a roughness density of $\lambda = 0.5$ (defined as the roughness frontal area per unit ground area). This difference in roughness length may be the result of the roughening of 2D building surfaces (with grit-impregnated paint) in the wind tunnel experiment of [8], in order to prevent re-laminarization of the flow on the building surfaces. For skimming flow over the 2D building array (analogous to a square bar array), where the normalized displacement height $d/H \gtrsim 0.9$ (which reflects the fact that the recirculation cavity between the obstacles is isolated from the main flow above the obstacle array), the roughness length z_0 in this case is more a measure of the momentum absorption by the “roughness” of the tops of the obstacles, rather than the roughness devolving from the individual array obstacle elements (square bars) themselves.

At $x = 1425$ mm, the modeled turbulence energy levels from both methods over-predict the measured TKE (by a factor of 2 at worst) as seen in Fig. 16. The overestimation of TKE in the region of the obstacle array where the mean flow within the canopy has become fully developed (approximately or better) may be due to the fact that the additional sink term in Eq. (25) arising from the presence of the obstacles only models the reduction in the TKE dissipation arising from the reduction in the TKE as the turbulent eddies do work against the form and viscous drag of the canopy elements. The increase in the dissipation rate due to the reduction of the turbulent mixing length scale within the canopy has not been properly modeled. It is conceivable that more comprehensive models for the inclusion of source/sink terms in the k - and ϵ -equations (as advocated by Antohe and Lage [24] and Getachew et al. [23]) may lead to better predictions in this case (albeit at the expense of much more complicated models).

Fig. 17 presents the distribution of the turbulence energy levels in the x - z plane predicted by the high-resolution CFD approach and the distributed drag force approach based on Methods (a) and (b). All the model predictions exhibit a zone with large production of TKE centered but displaced slightly upwards of the windward edge of the roof of the first building. However, for the distributed drag force approach, the TKE generated in this zone is “exported” (by mean advection or turbulent diffusion) much more readily into the “urban” canopy than for the high-resolution CFD simulation where the obstacles are explicitly resolved. Hence, a TKE “plume” extends downstream of the zone of maximum TKE production, but the damping of the TKE with downstream distance and within the canopy appears to be too small for the two distributed drag force models. This problem is most serious for Method (b) where all the obstacles between the first and last buildings are represented as a single drag unit. However, in Method (a), the large values of C_D assigned to the first and second drag units (cf. Fig. 11) result in significant dissipation of TKE within the “urban” canopy with the result that the TKE at these locations are actually under-predicted by the model (cf. Figs. 13 and 14).

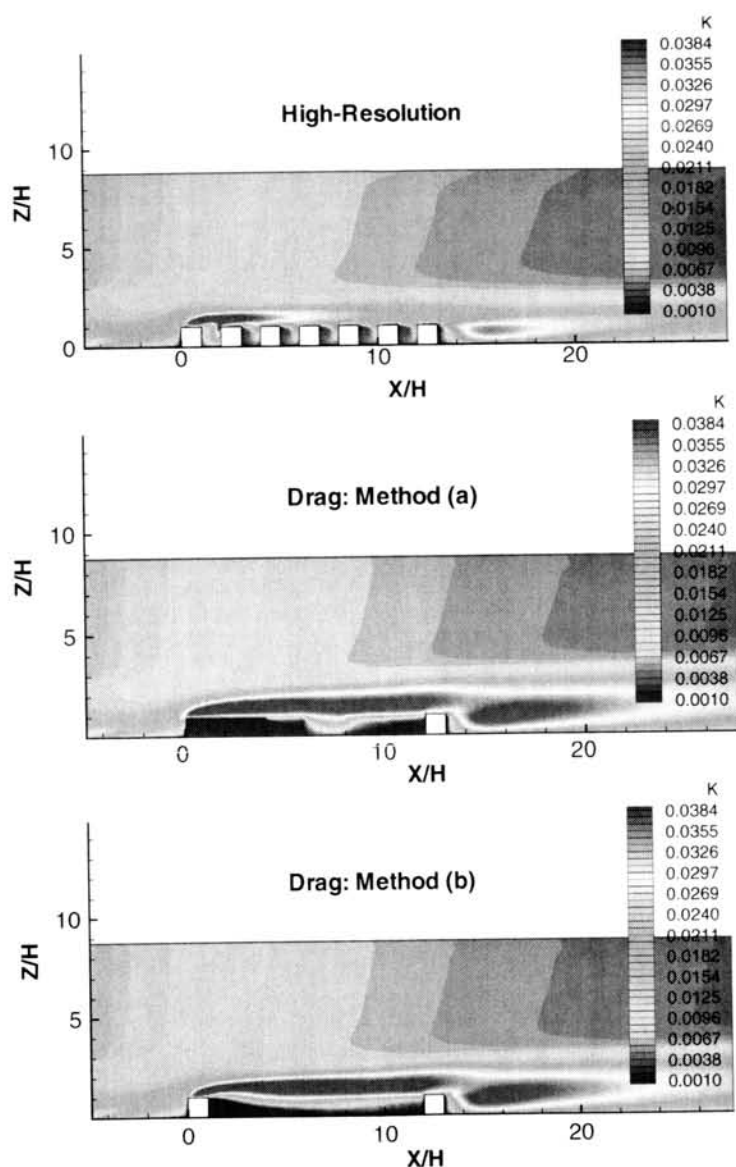


Fig. 17. Turbulence kinetic energy isopleths over the 2D array, obtained using a high-resolution numerical simulation and distributed drag force approach, are compared.

4.4. Dispersive stresses in the 2D building array

The high-resolution CFD simulations of the time-averaged flow within and over the 2D building array (cf. Section 3) can be used to diagnose the dispersive stresses in

this array. The dispersive stresses in the urban canopy arise from the spatial correlations in the point-to-point variations in the time-averaged (mean) velocity field. The dispersive stresses can be diagnosed from the time-mean velocity field determined from the high-resolution CFD simulation as follows. In this section only, it is necessary to distinguish explicitly the time averaging operation from the spatial-averaging operation. To this end, overbars will be used to denote time averaging whereas angular brackets will be used to denote spatial averaging. The dispersive normal and shear stresses for the 2D building array [cf. Fig. 10(a)] can be diagnosed from the time-mean velocity field \bar{u}_i , respectively, as follows:

$$\langle \bar{u}'' \bar{u}'' \rangle(z) \equiv \frac{1}{N} \sum_{\alpha=1}^N (\bar{u}_{(\alpha)}(z) - \langle \bar{u} \rangle(z))^2 \quad (32)$$

and

$$\langle \bar{u}'' \bar{w}'' \rangle(z) \equiv \frac{1}{N} \sum_{\alpha=1}^N (\bar{u}_{(\alpha)}(z) - \langle \bar{u} \rangle(z))(\bar{w}_{(\alpha)}(z) - \langle \bar{w} \rangle(z)). \quad (33)$$

In Eqs. (32) and (33), $\bar{u} \equiv \bar{u}_1$ and $\bar{w} \equiv \bar{u}_3$ are the streamwise and vertical mean velocities, respectively; z is the height above the ground surface at which the velocity is evaluated; a double prime is used to denote a departure from the spatial average; N is the number of vertical profiles of time-mean velocity in a drag unit [cf. Fig. 10(a)] used in the construction of the spatial average; and the Greek subscript α enclosed in round brackets is used to denote a running index for the vertical profiles of time-mean velocity in a drag unit (and, should not be confused with the Roman subscript index i used to distinguish a component of the velocity). The angular brackets in Eqs. (32) and (33) refer explicitly to a spatial average over a drag unit of the urban array. More specifically, to resolve the variation of the dispersive and spatially averaged Reynolds stresses in the vertical (or z -) direction, the averaging volume implied by the angular brackets is taken to be an infinitesimally thin horizontal slab through the drag unit.

Figs. 18 and 19 exhibit the normal and shear dispersive stresses, respectively, for drag units #1 to #6 in the 2D building array. The normal and shear dispersive stresses have been compared with the spatially averaged normal and shear Reynolds stresses (denoted by $\langle \bar{u}' \bar{u}' \rangle$ and $\langle \bar{u}' \bar{w}' \rangle$, respectively, where the single prime indicates a departure from the time-averaged value). The quantities $\langle \bar{u}' \bar{u}' \rangle$ and $\langle \bar{u}' \bar{w}' \rangle$ represented by the solid lines in Figs. 18 and 19 were determined by spatially averaging the Reynolds stresses (obtained from the high-resolution CFD simulation) over thin horizontal slabs through the various drag units (or, averaging units) shown in Fig. 10(a). Interestingly, for the 2D building array, the normal and shear dispersive stresses are comparable in magnitude to the associated spatially averaged Reynolds stresses in drag unit #1 for $1 \lesssim z/H \lesssim 2$, but appear to be negligible above canopy height ($z/H > 1$) in the drag units further downstream. Furthermore, the dispersive shear stress here is opposite in sign to the Reynolds shear stress. For drag units #3 to #6, the normal dispersive stress is larger than the normal Reynolds stress within the urban canopy for the height ranges $2/3 \lesssim z/H \lesssim 1$ and $0 \lesssim z/H \lesssim 1/3$. Note

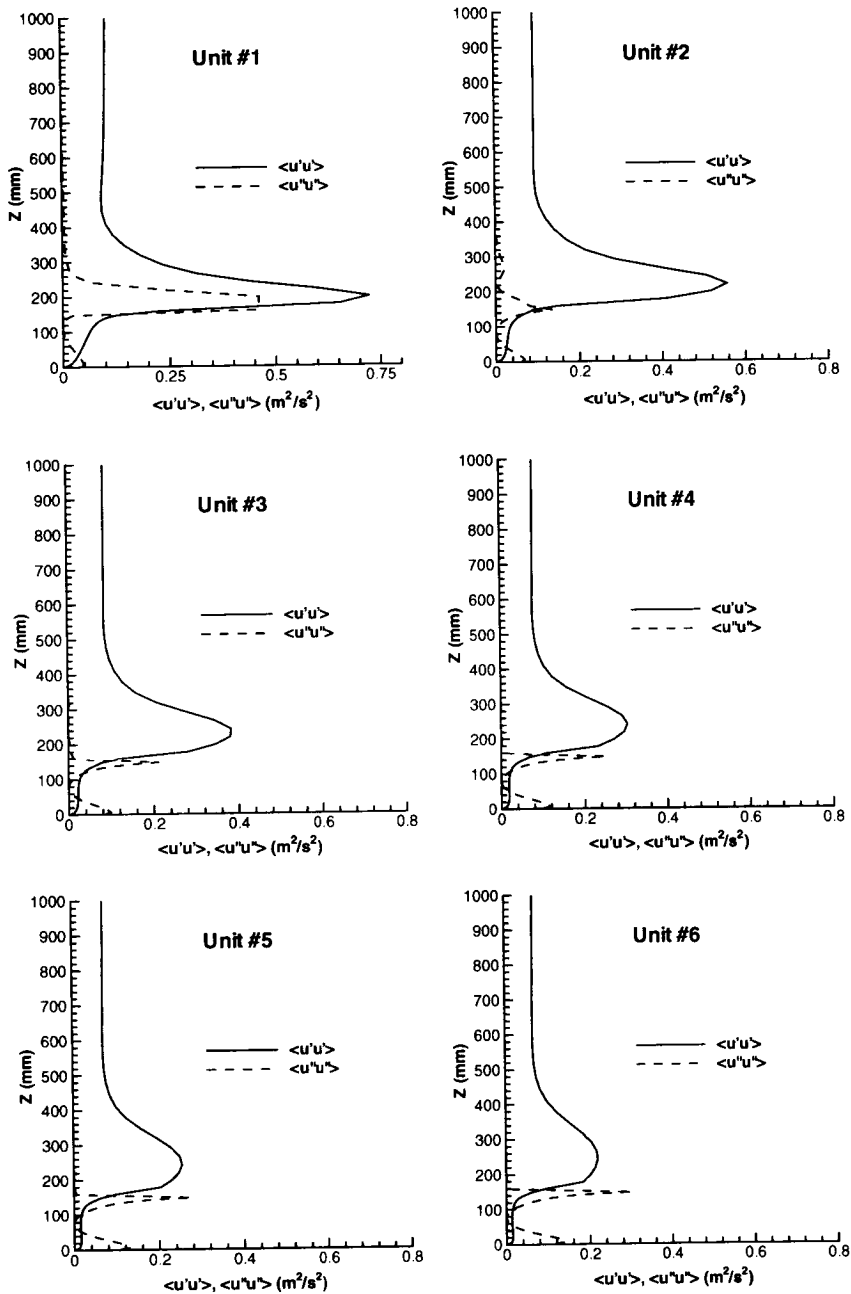


Fig. 18. Comparison between the Reynolds normal stress $\langle \overline{u'u'} \rangle$ (solid line) and the dispersive normal stress $\langle \overline{u''u''} \rangle$ (dashed line) in the 2D building array for drag units #1 to #6.

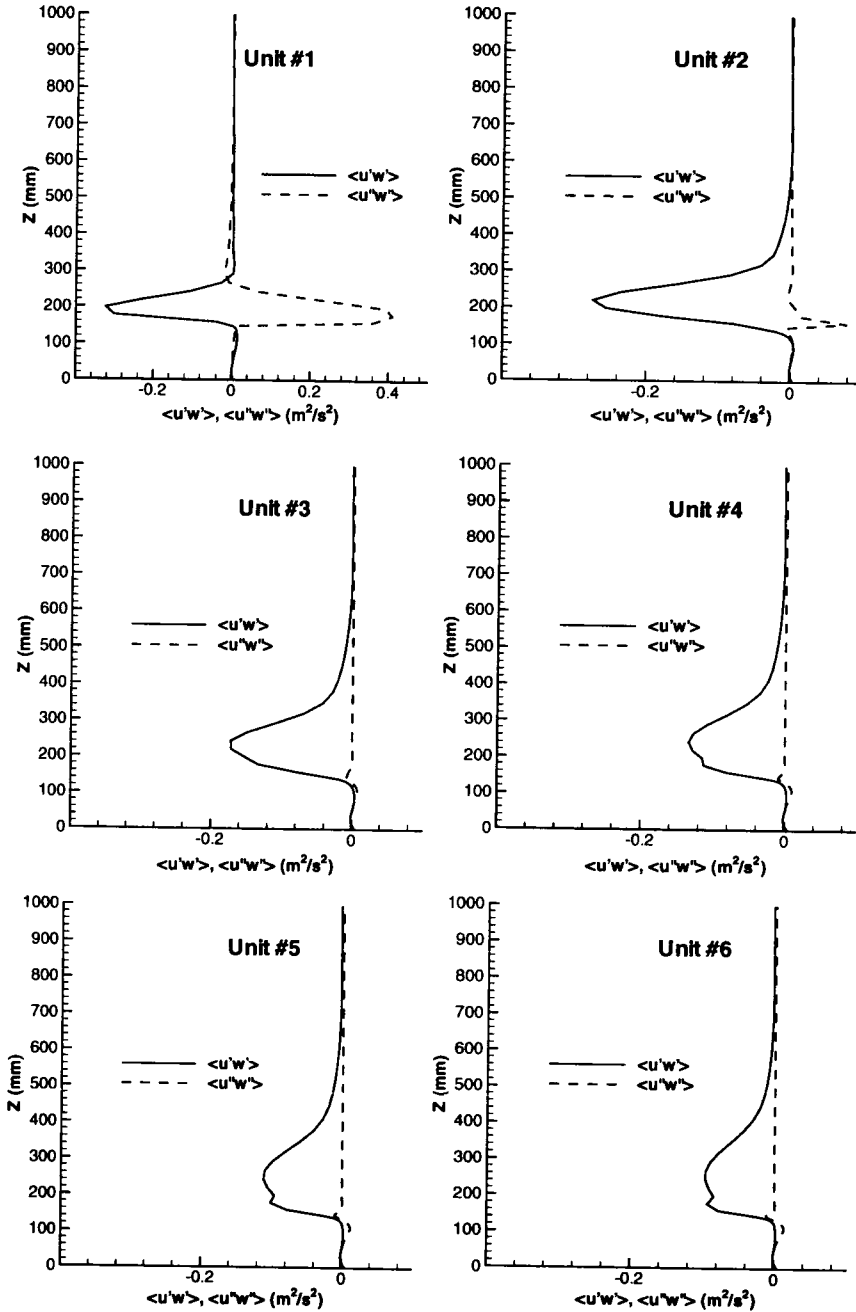


Fig. 19. Comparison between the Reynolds shear stress $\langle u'w' \rangle$ (solid line) and the dispersive shear stress $\langle u''w'' \rangle$ (dashed line) in the building array for drag units #1 to #6.

that for the 2D building array with skimming flow over the array, both the spatially averaged Reynolds normal and shear stresses tend to be very small within the urban canopy ($z/H < 1$). For the 2D building array in the skimming flow regime, both the dispersive and spatially averaged Reynolds shear stresses are negligible within the urban canopy.

5. Summary and conclusions

A number of variants of the $k-\epsilon$ turbulence-closure model, applied with wall functions, has been used to calculate the disturbed mean flow and turbulence through and above an array of two-dimensional buildings. It should be emphasized that for these numerical simulations, the closure constants in the $k-\epsilon$ turbulence model retained their original (standard) values. In consequence, all model predictions were obtained without adjustment of any of the closure constants. This ensures that the process did not simply degenerate into a “curve-fitting” exercise. The primary purpose of this effort was to assess critically the model’s predictive performance by comparison of the mean flow and turbulence statistics with a very comprehensive and detailed wind tunnel simulation. In addition, the results of the high resolution CFD simulation based on the $k-\epsilon$ turbulence models were used also to diagnose drag coefficients that can be used in a distributed drag force representation of the obstacle array. The utility of using a distributed drag force representation of an obstacle or group of obstacles in the array for the prediction of the disturbed flow has been investigated.

The comparison of predicted (using high-resolution CFD simulations) and measured streamwise velocity profiles indicated that most of the qualitative features of the mean flow field—such as speed-up over the first building rooftop, the presence of a thin separation layer near the surface of the first rooftop and the absence of such a feature in all the succeeding rooftops, the standing vortex in the street canyon, the thin strong shear layer that forms at building height, the recirculation zone behind the last building, the development of the mixing layer above and downstream of this recirculation zone, and the rate of momentum recovery in the far wake region—are correctly predicted. The quantitative agreement is also fairly good throughout most of the flow domain for the mean streamwise velocity.

The turbulence kinetic energy from the high-resolution numerical and physical simulations show striking resemblances and, indeed, most of the qualitative features of the turbulence energy as it develops through and above the array of buildings are adequately predicted. In terms of quantitative agreement, it is found that the TKE level is generally underestimated by the model. This underestimation may be caused by the inability of the model to capture the disproportionate and inhomogeneous sensitivity of the Reynolds stress components to secondary strains in the flow, particularly those associated with curvature. Specifically, the production of TKE just upstream and above the first building arising from the mean streamline concave (destabilizing) curvature strain here and from the “flapping” of the shear layer, is not adequately captured by the model. Because the TKE is exported downstream

and vertically by advection and by turbulent and/or pressure diffusion, the under-prediction of the TKE at and near the leading edge of the first building (i.e., the location where the turbulence energy production is greatest) will result in reduced TKE levels at all positions downstream of this location.

It has been shown how a high-resolution CFD simulation model can be applied to determine the drag force in a given control volume of the obstacle array and how this information can be used to diagnose the values of the drag coefficient C_D required in a distributed drag force representation of the obstacles in the array. These diagnosed values of C_D have been used in various drag force models of the obstacle array, and have been compared to detailed measurements of the horizontally averaged mean velocity and turbulence energy levels in the array. It was found that the numerical simulations based on the distributed drag force approach were able to satisfactorily predict most of the main characteristics of the mean streamwise velocity, and many of the relevant features of the TKE. However, although many of the qualitative features of the flow around and within the obstacle array were correctly simulated with the distributed drag force approach, the complicated details relating to the local heterogeneity of the flow cannot be predicted. For the latter, a high-resolution CFD simulation is required.

The standard or K - L k - ϵ turbulence-closure model with an isotropic, linear eddy viscosity is perhaps the simplest complete turbulence model (viz., no advance knowledge of any property of the turbulence is required for the simulation other than the initial and/or boundary conditions for the problem) that is available currently, and its moderately good predictive performance of the complicated developing flow through an array of two-dimensional buildings without the need to adjust any closure constants is encouraging. This model may be useful as a general purpose simulator of urban flows since it is simple enough to be tractable numerically and, hence, not require excessive computing time. However, if a better representation of mean velocity and turbulence fields is required in the vicinity of a cluster of buildings, then the non-linear k - ϵ model is recommended. The latter model is slightly more complicated than the standard k - ϵ model, and requires between about 10 and 20 percent more computational effort than the standard k - ϵ model to provide a prediction for the flow. It is conceivable that these numerical simulation models could provide all the statistics of the disturbed wind flow in a building cluster required as input to a physically based model for the prediction of dispersion of contaminants in the array.

References

- [1] D.A. Paterson, C.J. Apelt, Computation of wind flows over three-dimensional buildings, *J. Wind Eng. Ind. Aerodyn.* 24 (1986) 193–213.
- [2] Y.Q. Zhang, A.H. Huber, S.P.S. Arya, W.H. Synder, Numerical simulation to determine the effects of incident wind shear and turbulence on the flow around a building, *J. Wind Eng. Ind. Aerodyn.* 46–47 (1993) 129–134.
- [3] Y. Zhou, T. Stathopoulos, A new technique for the numerical simulation of wind flow around buildings, *J. Wind Eng. Ind. Aerodyn.* 72 (1997) 137–147.

- [4] I.R. Cowan, I.P. Castro, A.G. Robins, Numerical considerations for simulations of flow and dispersion around buildings, *J. Wind Eng. Ind. Aerodyn.* 67–68 (1997) 535–545.
- [5] R. Lee, A finite element/finite difference approach for modeling three-dimensional flow and pollutant dispersion around structures, Report UCRL-J-10775 DE92 019377, Lawrence Livermore National Laboratory, Livermore, CA, 1992.
- [6] L.J. Hunter, I.D. Watson, G.T. Johnson, Modeling air flow regimes in urban canyons, *Energy Build.* 15–16 (1990/91) 315–324.
- [7] R.P. Hosker, Flow around isolated structures and building cluster: a review, *ASHRAE Trans.* 91 (2B) (1985) 1671–1692.
- [8] M.J. Brown, R.E. Lawson, D.S. Decroix, R.L. Lee, Mean flow and turbulence measurements around a 2-D array of buildings in a wind tunnel, Proceedings of the 11th Joint AMS/AWMA Conference on the Application of Air Pollution Meteorology, Long Beach, CA, USA, LA-UR-99-5395, 2000.
- [9] S.B. Pope, A more general effective-viscosity hypothesis, *J. Fluid Mech.* 72 (1975) 331–340.
- [10] W.P. Jones, B.E. Launder, The prediction of laminarisation with a two-equation model of turbulence, *Int. J. Heat Mass Transfer* 15 (1972) 301–314.
- [11] M. Kato, B.E. Launder, The modeling of turbulent flow around stationary and vibrating square cylinders, Proceedings of the Ninth Symposium on Turbulent Shear Flows, Kyoto, Japan, 1993.
- [12] V. Yakhot, S. Orzag, S. Thangam, T.B. Gatski, C.G. Speziale, Development of turbulence models for shear flows by a double expansion technique, *Phys. Fluids A* 7 (1992) 1510–1520.
- [13] T.H. Shih, J. Zhu, J.L. Lumley, A realizable Reynolds stress algebraic equation model, NASA TM-105993, National Aeronautics and Space Agency, 1993.
- [14] P.A. Durbin, B.A. Pettersson Reif, *Statistical Theory and Modeling for Turbulent Flows*, Wiley, New York, 2001.
- [15] B.P. Leonard, A stable and accurate convective modeling procedure based on quadratic upstream interpolation, *Comput. Meth. Appl. Mech. Eng.* 19 (1979) 59–98.
- [16] S.V. Patankar, *Numerical Heat Transfer and Fluid Flow*, Hemisphere Publishing Corporation, New York, 1980.
- [17] C.M. Rhie, W.L. Chow, Numerical study of the turbulent flow past an airfoil with trailing edge separation, *AIAA J.* 21 (1983) 1525–1532.
- [18] F.S. Lien, M.A. Leschziner, A general non-orthogonal finite-volume algorithm for turbulent flow at all speeds incorporating second-moment closure, Part 1: numerical implementation, *Comput. Meth. Appl. Mech. Eng.* 114 (1994) 123–148.
- [19] P. Louka, S.E. Belcher, R.G. Harrison, Coupling between air flows in streets and the well-developed boundary layer aloft, *Atmos. Environ.* 34 (2000) 2613–2621.
- [20] F.S. Lien, M.A. Leschziner, Modeling 2D separation from high-lift aerofoil with nonlinear eddy-viscosity model and second-moment closure, *Aeronaut. J.* 99 (1995) 125–144.
- [21] F.S. Lien, M.A. Leschziner, Computational modeling of multiple vortical separation from streamlined body at high incidence, *Aeronaut. J.* 101 (1997) 269–275.
- [22] S.E. Belcher, N. Jerram, J.C.R. Hunt, Adjustment of a turbulent boundary layer to a canopy of roughness elements, *J. Fluid Mech.* 488 (2003) 369–398.
- [23] D. Getachew, W.J. Minkowycz, J.L. Lage, A modified form of the k - ϵ model for turbulent flows of an incompressible fluid in porous media, *Int. J. Heat Mass Transfer* 43 (2000) 2909–2915.
- [24] B.V. Antohe, J.L. Lage, A general two-equation macroscopic turbulence model for incompressible flow in porous media, *Int. J. Heat Mass Transfer* 40 (1997) 3013–3024.
- [25] K.W. Ayotte, J.J. Finnigan, M.R. Raupach, A second-order closure for neutrally stratified vegetative canopy flows, *Boundary-Layer Meteorol.* 90 (1999) 189–216.
- [26] M.R. Raupach, P.A. Coppin, B.J. Legg, Experiments on scalar dispersion within a model plant canopy, part I: the turbulence structure, *Boundary-Layer Meteorol.* 35 (1986) 21–52.
- [27] H. Cheng, I.P. Castro, Near wall flow over urban-like roughness, *Boundary-Layer Meteorol.* 194 (2002) 229–259.
- [28] K. Lee, J.R. Howell, Forced convective and radiative transfer within a highly porous layer exposed to a turbulent external flow field, Proceedings of the ASME-JSME Thermal Engineering Joint Conference, Washington, DC, USA, 1987.

- [29] S.-J. Lee, H.-C. Lim, A numerical study on flow around a triangular prism located behind a porous fence, *Fluid Dyn. Res.* 28 (2001) 209–221.
- [30] A.R. Packwood, Flow through porous fences in thick boundary layers: comparisons between laboratory and numerical experiments, *J. Wind Eng. Ind. Aerodyn.* 88 (2000) 75–90.
- [31] J.D. Wilson, Numerical studies of flow through a windbreak, *J. Wind Eng. Ind. Aerodyn.* 21 (1985) 119–154.
- [32] N.R. Wilson, R.H. Shaw, A higher-order closure model for canopy flow, *J. Appl. Meteorol.* 16 (1977) 1198–1205.
- [33] T. Meyers, K.T. Paw U, Testing of a higher-order closure model for modeling airflow within and above plant canopies, *Boundary-Layer Meteorol.* 37 (1986) 297–311.
- [34] M.R. Raupach, R.H. Shaw, Averaging procedures for flow within vegetation canopies, *Boundary-Layer Meteorol.* 22 (1982) 79–90.
- [35] J. Finnigan, Turbulence in plant canopies, *Annu. Rev. Fluid Mech.* 32 (2000) 519–571.
- [36] J.D. Wilson, A second-order closure model for flow through vegetation, *Boundary-Layer Meteorol.* 42 (1988) 371–392.
- [37] M. Brown, M. Williams, An urban canopy parameterization for mesoscale meteorological models, *Proceedings of the Second AMS Urban Environment Symposium*, Albuquerque, New Mexico, USA, LA-UR-98-3831, 1998.
- [38] T. Vu, A. Yasunobu, T. Asaeda, A k - ϵ turbulence closure model for the atmospheric boundary layer including urban canopy, *Boundary-Layer Meteorol.* 102 (2002) 459–490.
- [39] A. Martilli, Development of an urban turbulence parameterization for mesoscale atmospheric models, Ph.D. Dissertation, École Polytechnique Fédérale de Lausanne, Lausanne, Switzerland, 2001.
- [40] Y. Brunet, J.J. Finnigan, M.R. Raupach, A wind tunnel study of air flow in waving wheat: single-point velocity statistics, *Boundary-Layer Meteorol.* 70 (1994) 95–132.
- [41] A.S. Thom, Momentum absorption by vegetation, *Q. J. R. Meteorol. Soc.* 97 (1971) 414–428.
- [42] M.R. Raupach, R.A. Antonia, S. Rajagopalan, Rough-wall turbulent boundary layers, *Appl. Mech. Rev.* 44 (1991) 1–25.

#521350
CA023856

